EQUILIBRIUM AND PHOTOKINETIC PROPERTIES OF PHENOLIC COMPOUNDS AT THE AIR-WATER INTERFACE

A THESIS

SUBMITTED TO THE GRADUATE SCHOOL

IN PARTIAL FULFILLMENT OF THE REQUIREMENTS

FOR THE DEGREE OF

MASTER OF SCIENCE

BY

DANIEL HEADLEY

DR. MAHAMUD SUBIR – ADVISOR

BALL STATE UNIVERSITY

MUNCIE, INDIANA

JULY 2016

ACKNOWLEDGEMENTS

I wish to convey my sincerest gratitude to my advisor, Dr. Mahamud Subir, for his dedication, guidance, support, understanding, candor, and integrity. His tireless pursuit of knowledge and his commitment to represent new information accurately and honestly are qualities that I hold in the highest regard. Furthermore, I wish to thank him for his faith in me, without which I may have never come this far.

I would like to thank the faculty and staff of the Department of Chemistry for all of the work that they do to ensure that students are well cared for, knowledge is conveyed thoroughly and coherently, and a positive learning environment is maintained.

I also wish to thank my thesis committee members, Dr. James Poole and Dr. Patricia Lang, for their patience and assistance in guiding me to a deeper understanding of the chemical and physical processes associated with this work. Their love of teaching and their scrupulous approach to research are traits that I hope to carry with me in my future endeavors.

I would like to thank my research group members for their support in this project. In particular, I wish to express my gratitude to Maggie Schmits and Ryan Young, as I may have never slept were it not for their assistance in completing this work. I would also like to thank Tyler Williams, whose ability to see new and better ways to approach problems, both inside and outside of the lab, I have the utmost admiration for.

I would like to thank Ball State University and the ACS Petroleum Research Fund for providing me with the means to explore this area of research.

Finally, I want to thank Jimmy, for always being understanding when I arrived late for dinner from the lab.

Table of Contents

List of Figures

Appendix

List of Tables

List of Equations

Chapter 1 **Motivations**

Chapter 1: Motivations

1.1 Introduction

The field of surface chemistry has risen in popularity in the years between the Nobel Prize winning achievements of Irving Langmuir in 1932 and Gerhard Ertl in 2007.[1] Even prior to 1932, scientists worked to discover new ways of utilizing the chemistry of surfaces through heterogeneous catalysis, but much of the work done was limited to the study of hard surfaces because the tools necessary to produce "clean" surfaces and investigate other types of surfaces were unavailable. Space exploration in the 1960s spurred scientists on to develop ultra-high vacuum (UHV) techniques for the production of cleaner surfaces.[2,3] Due to these developments, surface science is now a broad field that incorporates many disciplines including physics, chemistry, and biology.

Due to the ubiquity of surfaces, the study of surface chemistry has lent itself to a wide variety of applications. Solar cells, computer chips, protective coatings, and adhesives must exhibit certain surface properties, which allow them to function in the manner intended.[1-3] The study of surfaces yields a deeper understanding of the fundamental physical processes and interactions occurring at interfaces, thereby providing insight that results in improvements to the production, versatility and efficiency of devices and materials. While the study of surfaces yields information about the physical properties of the surface, it can also uncover chemical characteristics. By studying the nature of chemical reactivity at surfaces, development of new reaction methods that permit greater control of chemical reactions may be promoted.[1,2]

With the development of new tools to study surfaces and the importance of interfacial phenomena to a wide range of scientific fields and applications, it is no small wonder that interfacial chemistry is increasing in popularity. In this chapter, a review of the theoretical background of the primary technique used in our investigation of the surface is presented and the motivations of the research project within the broader literature are discussed.

1.2 Second-Harmonic Generation Spectroscopy

SHG spectroscopy is an effective tool in the study of chemical surfaces in that it is applicable to a number of different types of interface. The technique is selective for anisotropic media, media with properties that are non-uniformly distributed with respect to their orientation, which is a defining characteristic of an interface. SHG is a second-order nonlinear optical process converting two photons, each of frequency ω, to a single photon of frequency 2ω via promotion through virtual states, $|v\rangle$, which are non-stationary states of the system taken as constructs used to describe the process using quantum mechanics.[4] Upon relaxation, the newly generated photon is therefore equal in energy to the sum of the energies of the two absorbed photons[5,6] (Fig. 1-1 & 1-2).

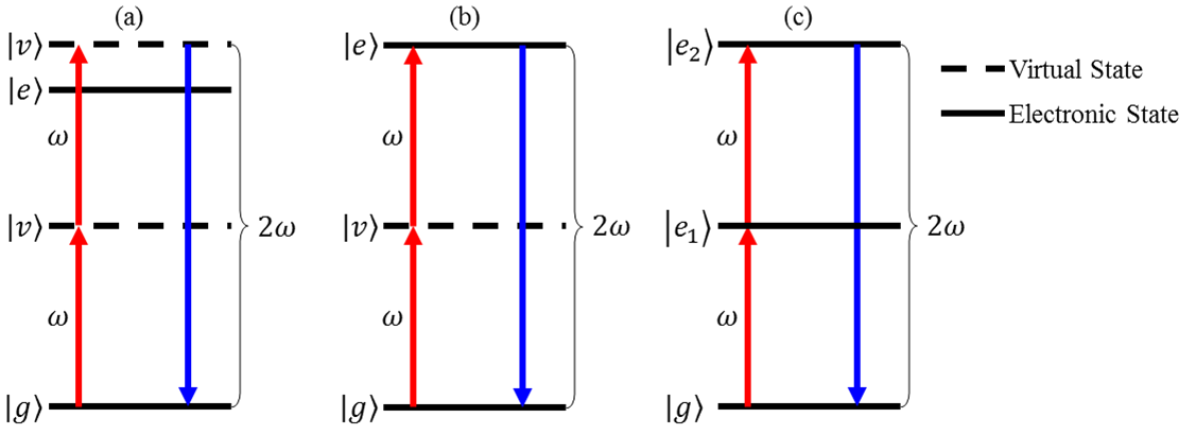

Figure 1-1: Energy level diagrams of SHG processes where two photons of frequency ω generate a single photon of frequency 2ω. $|g\rangle$ and $|e\rangle$ are the ground and excited electronic states of the molecule, respectively, and $|v\rangle$ represents virtual states, which are transient states of indeterminate energy. Diagram (a) is a nonresonant case where the molecular transition frequency does not overlap significantly with the fundamental or SH frequency. Diagram (b) shows a molecular transition that is singly resonant at the SH frequency and diagram (c) represents a molecule with two excited energy states that are resonant with both the fundamental and SH frequency.

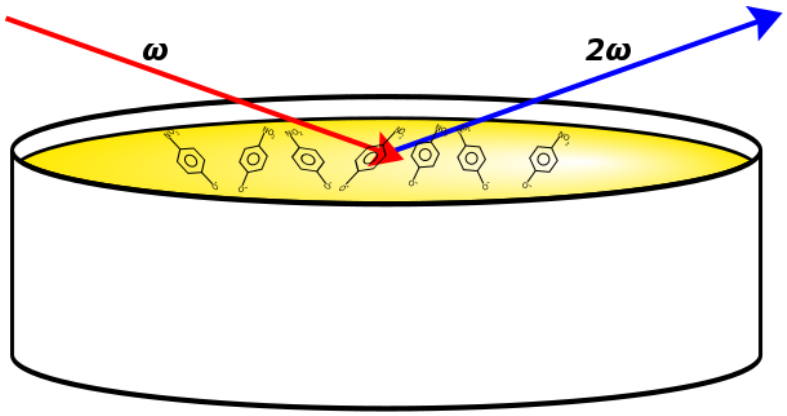

Figure 1-2: The SHG process occurs when the fundamental beam interacts with noncentrosymmetric media. This diagram shows the fundamental beam striking the surface of a solution of p-nitrophenolate and generating the SH signal.

The manner in which the photons interact with a molecule with respect to molecular transitions determines the intensity of the second-harmonic (SH) signal produced. Eq. 1-1 represents this relationship, where $\beta_{ijk}^{(2)}$, a second-order molecular hyperpolarizability tensor referenced to the molecular coordinates i, j, and k, is expressed as a sum over states. The bra-kets in the numerator refer to the probabilities of transition between states, where $\vec{\mu}_j$ and $\vec{\mu}_k$ are the transition dipole moments associated with fundamental frequency, ω, and $\vec{\mu}_i$ is the transition dipole moment associated with the SH frequency, 2ω. The frequency terms, ω_{gv} and ω_{eg}, represent a molecular transition occurring near the fundamental and SH frequencies, respectively. It is important to note that these terms are not represented in Fig. 1-1 as the transition between the ground and excited state of the molecule does not have to overlap with the transitions associated with the virtual states. This does not mean, however, that SHG cannot take place, but that it will not be resonantly enhanced. Lastly, Γ_{gv} and Γ_{eg} are lifetime broadening terms which arise from uncertainty in the energy.[5-13]

$$\beta_{ijk}^{(2)}(2\omega;\omega,\omega) = \sum_{g,e} \frac{\langle g|\vec{\mu}_j|v\rangle\langle v|\vec{\mu}_k|e\rangle\langle e|\vec{\mu}_i|g\rangle}{(\omega - \omega_{gv} + i\Gamma_{gv})(2\omega - \omega_{eg} + i\Gamma_{eg})} \qquad \text{(Eq. 1-1)}$$

From Eq. 1-1, as the frequency of either the fundamental or SH beam approaches the frequency of a molecular transition, the hyperpolarizability tensor increases. The diagram in Fig. 1-1(a) depicts a non-resonant case where there is no appreciable overlap between the frequency of the molecular transition and either the fundamental or SH frequency. A case where there is significant overlap at one (Fig. 1-1(b)) or both of the virtual states (Fig. 1-1(c)) would represent a molecule that is either singly or doubly resonant with the laser source and would result in an increase in the number of photons generated at the SH frequency.

While the hyperpolarizability tensor yields insight into the molecular picture of SHG, it is also important to consider the macroscopic property to which it relates. When the hyperpolarizability tensors in the molecular frame are resolved into the laboratory frame and multiplied by the number of adsorbed molecules, N_s, they return the $\chi^{(2)}_{IJK}$ second-order susceptibility tensor elements (Eq. 1-2).[5,6,14-17] In this equation, the $R_{\Lambda\lambda'}$ terms represent elements of the Euler coordinate transformation, where I, J, K, are unit vectors in the laboratory frame and i, j, k, are unit vectors in the molecular frame.

$$\chi^{(2)}_{IJK} = N_s \sum_{i'j'k'=x'y'z'} \langle R_{Ii'} R_{Jj'} R_{Kk'} \rangle \beta^{(2)}_{i'j'k'} \qquad \text{(Eq. 1-2)}$$

As a generalization, this equation relates the macroscopic second-order susceptibility term to both the number of molecules adsorbed to a surface and, $\langle \beta^{(2)} \rangle$, the second order hyperpolarizability averaged over molecular orientation with respect to the laboratory frame (Eq. 1-3).[5,6,12,14,15,17-21] When written in this manner, this relation highlights two of the surface properties that much of our work will focus on.

$$\chi^{(2)} \propto N_s \langle \beta^{(2)} \rangle \qquad \text{(Eq. 1-3)}$$

While the preceding discussion details two of the major considerations for this work, it is also important to understand why SHG is effective for selectively studying chemical surfaces. It

is therefore necessary to understand that molecules at surfaces experience the dielectric characteristics of the two media at the interface and that these adsorbed molecules align themselves with a measurable average orientation with respect to the surface normal. In Fig. 1-3, the dipoles represent solute molecules with an affinity to the interface, such that the driving force is towards the surface. Upon adsorption, the molecules align with an average orientation with respect to the surface normal. In this case, both the air and bulk solution are isotropic, meaning that the dipoles of the solute and solvent molecules are randomly distributed such that the net dipole moment of the bulk solution is zero. In contrast, the line on the graph depicting the solution surface has a net nonzero dipole moment, making the surface anisotropic.

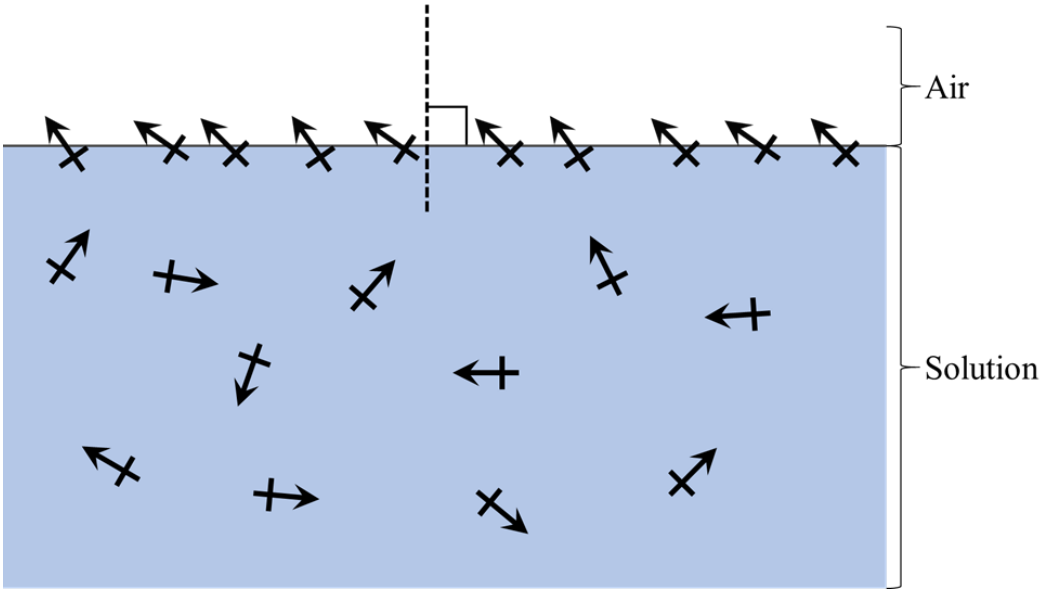

Figure 1-3: Basic representation of molecules adsorbed to a solution surface. Molecules from bulk solution are driven to the air-water interface where they align with an average molecular orientation with respect to the surface normal, an imaginary line perpendicular to the plane of the surface represented by a dashed line in the figure.

This surface anisotropy is what makes SHG surface selective. To demonstrate this, consider induced polarization as a Taylor expansion (Eq. 1-4).

$$\vec{P} = \vec{P}_0 + \chi^{(1)} \cdot \vec{E} + \chi^{(2)} : \vec{E}\vec{E} + \chi^{(3)} \vdots \vec{E}\vec{E}\vec{E} \ldots \quad \text{(Eq. 1-4)}$$

In equation 4, the induced polarization, $\vec{P}$, is expressed in terms of applied electric field vectors, $\vec{E}$, and susceptibility terms relating to different optical processes, $\chi^{(n)}$. For example, $\chi^{(1)}$, the first-

order term, relates to linear spectroscopies and gives rise to properties such as the refractive index of a material. SHG, however, relates to the second-order susceptibility term, which is isolated to obtain Eq. 1-5.[5,9,14,17,19,22-24] The physical interpretration of this is that an ensemble of oscillators interacts with two in phase electric fields which correspond to the electric field components of two photons from the fundamental beam. This interaction between light and matter will effect a second-order induced polarization, $\vec{P}^{(2)}$, in the oscillators if the susceptibility term is greater than zero.

$$\vec{P}^{(2)} = \chi^{(2)} : \vec{E}\vec{E} \qquad \text{(Eq. 1-5)}$$

Consider an isotropic material, characterized as having uniformly distributed microscopic forces that result in a macroscopic net force of zero, and apply the inversion operator (Eq. 1-6, 1-7, & 1-8).

$$\hat{\imath}\vec{P}^{(2)} = \hat{\imath}\chi^{(2)} : \vec{E}\vec{E} \qquad \text{(Eq. 1-6)}$$

$$-\vec{P}^{(2)} = \chi^{(2)} : -\vec{E} - \vec{E} \qquad \text{(Eq. 1-7)}$$

$$-\vec{P}^{(2)} = \chi^{(2)} : \vec{E}\vec{E} \qquad \text{(Eq. 1-8)}$$

By applying the inversion operator, all vector quantities become negative. It follows that for Eq. 1-5 and 1-8 to be true, the value of $\chi^{(2)}$ must be zero for isotropic media. However, in anisotropic materials, such as surfaces or crystalline materials, the value of $\chi^{(2)}$ does not become zero because the forces experienced by the molecules will vary from axis to axis, thereby allowing SHG to take place. As it pertains to the study of the air-water interface, this means that the SH signal observed from the experiment is generated by the surface itself or by molecules adsorbed to it.

A goal of the research project has been to utilize this tool to develop a fundamental understanding of the equilibrium and photochemical properties exhibited by phenolic compounds at the aquatic surface. SHG spectroscopy is therefore an effective tool to this end. While the

theoretical background presented here is not comprehensive, it does provide an understanding of how this tool applies to our system.

1.3 Phenolic Compounds in the Aqueous Environment

According to the United States Geological Survey (USGS) and National Aeronautics and Space Administration (NASA) 71-75% of the surface of the Earth is water covered.[25,26] With so much of the Earth covered in water, the air-water interface is ubiquitous. It is therefore important to develop an understanding of the chemical processes that occur at this interface.

Phenolic compounds are a class of organic compounds used in or produced by a number of industrial processes and applications. Their widespread use in petrochemical,[27-29] agrochemical,[29,30] pharmecutical,[28-30] and other industries[27-32] ultimately results in these compounds making their way into the aquatic environment.

1.3.1 Phenolic Compounds at the Air-Water Interface

Not only do these compounds find their way into waterways, but they also have an affinity for the air-water interface. SHG experiments on the adsorption of neutral phenol[11,19,33,34] and p-nitrophenol[9-11,19,20,35] (PNP) show that these compounds adsorb to the solution surface. In 1988, Bhattacharyya *et al.* showed that charged phenolates will adsorb to the air-water interface if an alkyl chain of sufficient length is attached to the molecule.[19,33,36] They initially postulated that without a significantly hydrophobic group attached to the molecule, the affinity of phenolate to the solution surface would not be great enough to drive these ions to the surface. However, in 2007, Minofar *et al.* simulated the adsorption of phenolate anions to the air-water interface and found that the process was favorable.[37] This was subsequently confirmed by collecting the sum-frequency spectrum of phenolate at the air-water interface.[34] This was a surprising result in that

ions would be expected to remain dissolved in solution due to favorable solvation of the anion in water.

In order to describe relative affinities of phenol, phenolate, and PNP to the aqueous surface, the Gibbs free energy of adsorption values obtained from both surface tension[11,34] and SHG experiments[10,33,38] are presented in Table 1-1. From these data, we may conclude that the neutral phenol has a greater affinity for the air-water interface than its conjugate anion, a reasonable conclusion as the anion is expected to be more solvated than is its neutral counterpart. Furthermore, PNP is shown to have a greater affinity for the air water interface than that of phenol, indicating that the nitro group also drives the molecule to the surface.

	ΔG_{ads} (kJ mol^{-1})	pH	Method Used
Phenol	-16±0.2	1	Surface Tension[34]
	-14.7±0.4	~7	Surface Tension[11]
	-15.9±0.1	x*	SHG[33]
	-16.1±0.3	1	SHG[38]
Phenolate	-7.9±0.3	13	SHG[38]
	-7.8±0.3	13	Surface Tension[34]
PNP	-16.4±0.2	~7	Surface Tension[11]
	-19	2	SHG[10]
	-21.13±0.08	1	SHG[38]

Table 1-1: Comparison of the Gibbs free energy of adsorption of phenolic compounds to the air-water interface. *The absent pH value is one for which the literature is unclear as to how the solution was prepared.

Literature is also available regarding the average and absolute orientation of phenol and PNP at the air-water interface. Using the nonlinear polarization sheet model of the surface (Appendix-I), a model which treats the refractive index of the surface as an average of the two interfacial media, Tamburello *et al.* reported the average molecular orientation, $\langle\theta\rangle$, of phenol to be 43° from the surface normal (Fig. 1-4) when dissolved in Millipore water.[11] In addition, they reported the average molecular orientation of PNP to be 48° from the surface normal under the same conditions.[11] At pH 2, Higgins *et al.* reported their determination of the average molecular orientation of PNP to be 55°,[10] also calculated using the nonlinear polarization sheet model. Bell

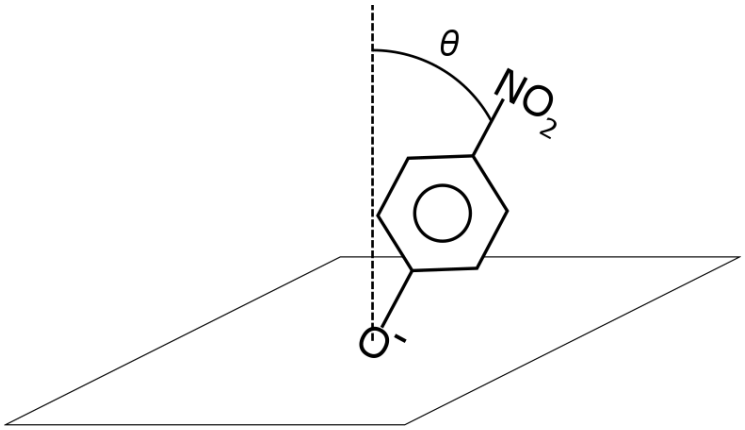

Figure 1-4: The surface normal is an imaginary line drawn perpendicular to the plane of the surface. Average molecular orientation is described by θ, the angle between the surface normal and the molecular axis.

et al. reported two different values for the molecular orientation of PNP about the surface normal. In their contribution, they did not use the nonlinear polarization sheet model, but assumed that adsorbed molecules reside either just above or just below the interface. For a solution of 100 mM PNP in 0.005 M HCl, approximately pH 2.3, they reported an average molecular orientation of 51° for the air layer and 38° for water.[35] Determinations of the absolute molecular orientation of both phenol[19] and PNP[9,10,19] at the aqueous surface indicate that the OH group is pointing down into the solution.

This data appears to suggest that phenol adsorbs to the interface in a more vertical alignment than PNP,[11] but variations in the experimental parameters between studies affect these calculations. Variations in the pH of the solutions shifts the equilibrium of each system such that the SH signal is not solely generated by either the neutral or the anionic species, but includes contributions from both (Fig. 1-5). The same holds true for the determination of their adsorption

Figure 1-5: Equilibrium of PNP and its conjugate anion. At pH 2 and pH 13, more than 99.9% of PNP in solution is either the neutral molecule or the conjugate anion, respectively.

affinities. Furthermore, the concentration of the solution may have an effect on the calculations of molecular orientation and it is unclear from the studies at which concentration these experiments were performed.[10,11]

1.3.2 Photodegradation of Phenolic Compounds

As a wastewater contaminant, phenolic compounds pose a health risk to organisms when ingested or absorbed through the skin and cell membranes,[28-32,39] and are known to bioaccumulate through the food chain. Furthermore, phenolic compounds are classified as priority pollutants by the EPA,[40,41] making their removal from wastewater a concern. While many methods of their removal from wastewater exist, our primary interest is that of UV photodegradation.

Irradiation by UV light offers a pathway to the removal of organic pollutants from environmental waters that is both cost effective and has low environmental impact.[27,29-31,39-46] There is a large volume of literature available about the photodecomposition of PNP utilizing UV-based advanced oxidative processes (AOPs), including photocatalysis with a variety of materials and methods.[27,29-32,39,41-45] Emphasis in the literature has been placed on investigating these AOPs, which are known to effectively and efficiently remove phenolic compounds from wastewater. In contrast, the direct UV photolysis of phenol and PNP has not been intensively studied as this process does not provide an effective means for the mineralization of organic pollutants. Nevertheless, information concerning the direct photolysis of these compounds can be gleaned from these resources and the few studies that concentrate on this process.[40,43,46-48]

Machalický *et al.* state that "quantum efficiency, $\varphi_{\Delta\lambda}$, is one of the most useful and fundamental quantities in the study of photochemical reactions."[49] That is to say, the rate of a photochemical reaction is dependent on the number of photons of each wavelength incident on the system investigated per second. This quantity, called the incident photon flux, q_p, varies between

light sources and experimental setups. Quantum efficiency calculations provide a way to quantitatively compare reaction rates between experiments under different laboratory conditions (Eq. 1-9). For this reason, we are interested in not only the reaction rate, but also the quantum efficiencies of the photolysis of PNP. In the equation, the reaction rate, r, is equal to the infinitesimal change in the concentration of the reactant with respect to time, $\frac{-d[A]}{dt}$. Photochemical rates are directly proportional to the quantum efficiency, $\varphi_{\Delta\lambda}$, a photon quantity that is an intensive property of the molecule describing the number of moles of reactant consumed per mole of photon (mol einstein^{-1}). The photokinetic of the reaction is also proportional to the product of the number of moles of photons incident on the sample per second, $q_{p,\lambda}$, and the fraction of light absorbed by the molecule, f_λ, at discrete wavelengths summed over the range, $\Delta\lambda$, per unit volume, V_r.

$$r = \frac{-d[A]}{dt} = \frac{\varphi_{\Delta\lambda} \sum_{\Delta\lambda} f_\lambda q_{p,\lambda}}{V_r} \qquad \text{(Eq. 1-9)}$$

It is important to note here, that the notation used in the literature differs from paper to paper. Machalický *et al.* state that quantum efficiency is used to describe photochemical rates over a range of wavelengths, essentially a weighted average, and that quantum yield, Φ, is used when describing irradiation by a single wavelength. Other sources use "quantum efficiency" and "quantum yield" synonymously and use only the notation, Φ. As this is the case, the notation used here is explicitly defined as it relates to the analysis of the system and review of the literature. The term quantum efficiency, $\varphi_{\Delta\lambda}$, is used to describe the quantum efficiency over a wavelength range, $\Delta\lambda$. Quantum yield, Φ_λ, is used when referring to a quantum yield at a specific wavelength and $\Phi(\lambda)$ when describing quantum yield as a function of wavelength.

Alif *et al.* provided the most comprehensive analysis of the quantum yield of PNP under different pH conditions and at different wavelengths.[47] In their analysis, the quantum yield of the photodegradation of PNP when irradiated by 365 nm light decreased with increasing pH. They

also showed that the quantum yield of PNP in acidic solution increased as the irradiation wavelength decreased, 4.1×10^{-5} mol einstein^{-1} at 365 nm and 6.0×10^{-4} mol einstein^{-1} at 253.7 nm. This is in good accordance with a study by Zhao *et al.* that compared the photokinetic of PNP when irradiated with light of 254 nm, 185 nm, and both wavelengths simultaneously.[48] Their determination was performed at pH 7 and is taken as comparative and not quantitative. They attributed the increased reaction rate to the formation of hydroxyl radicals from the decomposition of water, as the reaction rate of the photodegradation with 185nm light was only slightly slower than the reaction rate when irradiated at both wavelengths. This is a reasonable conclusion, as water does not absorb a significant amount light at 254 nm. A more quantitative analysis of the photolysis of PNP was performed by Bing *et al.* who reported a quantum efficiency of 7.94×10^{-4} mol einstein^{-1} over an irradiation range of 200 to 400 nm when irradiated by a polychromatic light source (1 kW medium pressure mercury lamp).[40]

Furthermore, the presence or absence of oxygen has a small effect on the quantum yield and reaction rate of the photolysis of PNP. Alif *et al.* reported a slight increase in the quantum yield of PNP in pH 2 solution when irradiated by 365 nm light in the absence of oxygen,[47] whereas Zhao *et al.* reported a decrease in the reaction rate when a pH 7 solution of PNP was irradiated by 254 nm light in the absence of oxygen.[46,48] Studies on the photolysis of phenol also report a similar trend with respect to pH: the anion is more photostable.[42] The quantum yield of phenol under irradiation by 254 nm light has been reported to decrease from 0.12 to 0.02 when the pH is increased from 1.6 to 13.2 with a minimum value at pH 11.1.

A number of mechanisms have been proposed to explain the photolysis of phenol[41,42,50] and PNP[40,46-48] into their photoproducts. In the case of PNP at pH 7, Bing *et al.* reported that after 15 min of irradiation, approximately 25% of the initial concentration of PNP had degraded.[40] The

percent yields of the photoproducts observed at a reaction progress of 25% are: 9.7% oxalate, 6.9% nitrite, 2.4% nitrate, 2.4% formic acid, 1.2% nitrocatechol, 0.5% phenol, and 0.4% maleic acid.[40] After 15 minutes, the concentration of phenol and maleic acid in solution begins to decrease but the concentration of nitrocatechol increases to a maximum at 30 minutes, at which point approximately 70% of the PNP in solution had degraded. This is in good agreement with the determinations made by Alif *et al.*[47] and Zhao *et al.*[46,48]. Variations in product formation exist in very acidic and very basic solution,[47] such that nitrohydroquinone is formed in small amounts when photodegraded in very acidic solution but not in basic solution. Furthermore, the concentration of nitrates formed from PNP photolysis in basic solution is lower than the concentrations produced from photolysis in acidic or neutral pH. In contrast, the observed concentration of nitrites formed by photodegradation is higher in alkaline conditions than either acidic or neutral pH.

The available literature appears to suggest that the degradation pathways for PNP are initiated by reaction with hydroxyl radicals generated from the decomposition of water molecules upon irradiation with light of very short wavelengths.[40,46-48] A mechanism for the reaction PNP with a hydroxyl radical was proposed by O'Neill *et al.* and includes pH considerations such that hydroxylation of the ring at the *ortho* and *para* positions is favored at low pH (Eq. 1-10), whereas denitration of the aromatic ring is favored in basic conditions (Eq. 1-11).[51] These mechanisms are in good agreement with the experimental observations of photoproduct formation in both acidic and basic conditions.[40,46-48,51,52] In the acidic reaction scheme, radical (II) and radical (I′) were reported as the stable protolytic forms due to the conjugation of the electrons on the O^- and nitro groups in radical (II) but not radical (I′).[51] These reaction schemes clarify how the photolysis process generates the nitrite photoproducts, as well as nitrocatechol in the acidic reaction. It also

depicts the formation of the radical precursor in the formation of benzoquinone in an alkaline environment. It is unclear as to how nitrohydroquinone is formed in acidic media from these schemes, however, it has been suggested that the ring is nitrated subsequent to these initial reactions.[47]

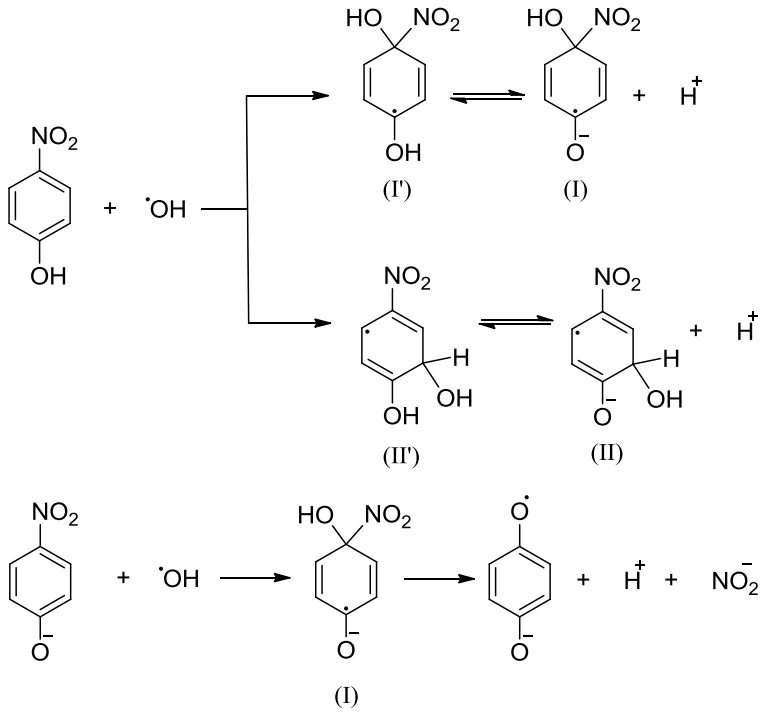

(Eq. 1-10)

(Eq. 1-11)

1.4 Research Goals

The research project in this study aims to augment our understanding of the adsorption of phenolic compounds to the air-water interface and to investigate the photochemistry of this surface (Fig. 1-6). PNP was selected as a target molecule for these investigations because its conjugate

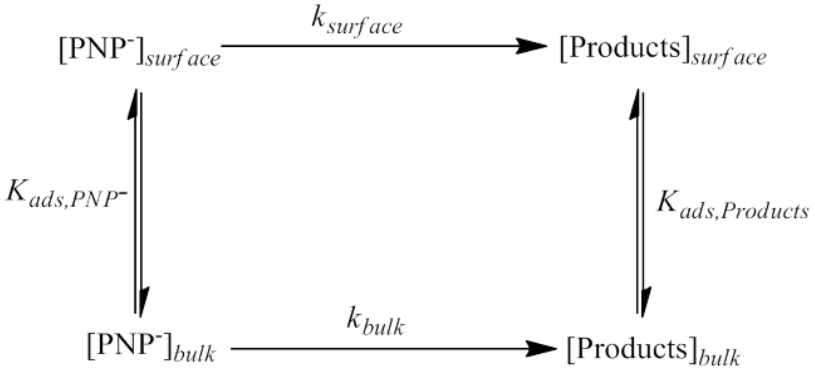

Figure 1-6: Representation of the photochemical behavior of PNP^- and its interactions with the surface. We are interested in both the surface equlibrium (K_{ads}) and surface photokinetic ($k_{surface}$).

anion, *p*-nitrophenolate (PNP^-), has an absorption maximum at 400 nm that is resonant with the laser. Presented here is a study that has systematically controlled the surface contributions by maintaining the equilibrium such that the surface is predominantly populated by either the neutral or the anionic species. Furthermore, a comparison of the bulk photodegradation of PNP^- to that of both bulk PNP and PNP^- at the surface is discussed.

References

(1) Yates, J. T.; Campbell, C. T. Surface chemistry: Key to control and advance myriad technologies. *Proceedings of the National Academy of Sciences* **2011**, *108*, 911-916.
(2) Somorjai, G. A.: *Introduction to surface chemistry and catalysis*; Wiley: New York, 1994.
(3) Somorjai, G. A.: *Principles of surface chemistry*; Prentice-Hall: Englewood Cliffs, N.J, 1972.
(4) Long, D. The Raman effect: a unified treatment of the theory of Raman scattering by molecules. 2002. West Sussex, England: John Wiley & Sons Ltd.
(5) Vidal, F.; Tadjeddine, A. Sum-frequency generation spectroscopy of interfaces. *Reports on Progress in Physics* **2005**, *68*, 1095.
(6) Moad, A. J.; Simpson, G. J. A unified treatment of selection rules and symmetry relations for sum-frequency and second harmonic spectroscopies. *The Journal of Physical Chemistry B* **2004**, *108*, 3548-3562.
(7) Campbell, D. J.; Higgins, D. A.; Corn, R. M. Molecular second harmonic generation studies of methylene blue chemisorbed onto a sulfur-modified polycrystalline platinum electrode. *Journal of Physical Chemistry* **1990**, *94*, 3681-3689.
(8) Simpson, G. J. New tools for surface second-harmonic generation. *Applied Spectroscopy* **2001**, *55*, 16A-16A.
(9) Corn, R. M.; Higgins, D. A. Optical second harmonic generation as a probe of surface chemistry. *Chemical reviews* **1994**, *94*, 107-125.
(10) Higgins, D. A.; Abrams, M. B.; Byerly, S. K.; Corn, R. M. Resonant second harmonic generation studies of p-nitrophenol adsorption at condensed-phase interfaces. *Langmuir* **1992**, *8*, 1994-2000.
(11) Tamburello-Luca, A. A.; Hebert, P.; Brevet, P. F.; Girault, H. H. Resonant-surface second-harmonic generation studies of phenol derivatives at air/water and hexane/water interfaces. *J. Chem. Soc., Faraday Trans.* **1996**, *92*, 3079-3085.
(12) Brevet, P. F.; Girault, H. H. Second harmonic generation at liquid/liquid interfaces. *Liquid-Liquid Interfaces: Theory and Methods. AG Volkov and DW Deamer, editors. CRC Press, Boca Raton, FL* **1996**, 103-137.
(13) Beildeck, C. L.; Liu, M. J.; Brindza, M. R.; Walker, R. A. Solvation of p-nitrophenol at a water/alkane interface: The role of ionic strength and salt identity. *The Journal of Physical Chemistry B* **2005**, *109*, 14604-14610.
(14) Gonella, G.; Dai, H.-L. Second harmonic light scattering from the surface of colloidal objects: Theory and applications. *Langmuir* **2013**, *30*, 2588-2599.
(15) Salafsky, J. S. Second-harmonic generation for studying structural motion of biological molecules in real time and space. *Physical Chemistry Chemical Physics* **2007**, *9*, 5704-5711.
(16) Eisert, F.; Gurka, M.; Legant, A.; Buck, M.; Grunze, M. Detection of molecular alignment in confined films. *Science* **2000**, *287*, 468-470.
(17) Shen, Y.-R. Principles of nonlinear optics. **1984**.
(18) Svechkarev, D.; Kolodezny, D.; Mosquera-Vázquez, S.; Vauthey, E. Complementary surface second harmonic generation and molecular dynamics investigation of the orientation of organic dyes at a liquid/liquid interface. *Langmuir* **2014**, *30*, 13869-13876.
(19) Eisenthal, K. Liquid interfaces probed by second-harmonic and sum-frequency spectroscopy. *Chemical Reviews* **1996**, *96*, 1343-1360.
(20) Bhattacharyya, K.; Sitzmann, E.; Eisenthal, K. Study of chemical reactions by surface second harmonic generation: p-Nitrophenol at the air–water interface. *The Journal of chemical physics* **1987**, *87*, 1442-1443.

(21) TamburelloáLuca, A. A. Surface second-harmonic generation at air/solvent and solvent/solvent interfaces. *Journal of the Chemical Society, Faraday Transactions* **1995**, *91*, 1763-1768.
(22) Shen, Y. Surface properties probed by second-harmonic and sum-frequency generation. *Nature* **1989**, *337*, 519-525.
(23) Heinz, T. F. Second-order nonlinear optical effects at surfaces and interfaces. *Nonlinear surface electromagnetic phenomena* **1991**, *29*.
(24) McGilp, J. Probing surface and interface structure using optics. *Journal of Physics: Condensed Matter* **2010**, *22*, 084018.
(25) How much water is there on and above the Earth? http://water.usgs.gov/edu/earthhowmuch.html (accessed May 19 2016).
(26) The water cycle. http://earthobservatory.nasa.gov/Features/Water/page1.php (accessed May 19 2016).
(27) Prabhu, K.; Shanmugapriya, S. Comparison of Efficiency of Solar Photocatalytic Degradation of Phenol using UV Transparent Materials. *International Journal of Engineering Science and Technology (IJEST)* **2012**, *4*, 1421-1425.
(28) Lee, S.; Kim, D.-J.; Choi, J.-W. Novel method for determination of phenol degradation kinetics. *Bioprocess and Biosystems Engineering* **2013**, *36*, 1939-1945.
(29) Islam, S.; Bormon, S. K.; Nadim, M.; Hossain, K.; Habib, A.; Islam, T. S. A. Photocatalytic Degradation of p-Nitrophenol (PNP) in Aqueous Suspension of TiO 2. *American Journal of Analytical Chemistry* **2014**, *2014*.
(30) Wu, Y.; Chen, R.; Liu, H.; Wei, Y.; Wu, D. Photo-Catalyzed p-Nitrophenol Degradation in Aqueous Dispersions of Ferrihydrite and H2O2. *Journal of nanoscience and nanotechnology* **2014**, *14*, 7325-7332.
(31) Lopes, P. R. M.; Montagnolli, R. N.; Bidoia, E. D. Analytical methods in photoelectrochemical treatment of phenol. *Journal of the Brazilian Chemical Society* **2011**, *22*, 1758-1764.
(32) Arana, J.; Melian, E. P.; López, V. R.; Alonso, A. P.; Rodríguez, J. D.; Díaz, O. G.; Pena, J. P. Photocatalytic degradation of phenol and phenolic compounds: Part I. Adsorption and FTIR study. *Journal of hazardous materials* **2007**, *146*, 520-528.
(33) Castro, A.; Bhattacharyya, K.; Eisenthal, K. B. Energetics of adsorption of neutral and charged molecules at the air/water interface by second harmonic generation: Hydrophobic and solvation effects. *The Journal of chemical physics* **1991**, *95*, 1310-1315.
(34) Rao, Y.; Subir, M.; McArthur, E. A.; Turro, N. J.; Eisenthal, K. B. Organic ions at the air/water interface. *Chemical Physics Letters* **2009**, *477*, 241-244.
(35) Andrew, J. Second harmonic generation by p-nitrophenol at water/air and water/heptane interfaces. *Journal of the Chemical Society, Faraday Transactions* **1992**, *88*, 2027-2030.
(36) Bhattacharyya, K.; Castro, A.; Sitzmann, E.; Eisenthal, K. Studies of neutral and charged molecules at the air/water interface by surface second harmonic generation: Hydrophobic and solvation effects. *The Journal of chemical physics* **1988**, *89*, 3376-3377.
(37) Minofar, B.; Jungwirth, P.; Das, M. R.; Kunz, W.; Mahiuddin, S. Propensity of formate, acetate, benzoate, and phenolate for the aqueous solution/vapor interface: Surface tension measurements and molecular dynamics simulations. *The Journal of Physical Chemistry C* **2007**, *111*, 8242-8247.
(38) Subir, M.: *Investigation of equilibrium and kinetic properties of charged and neutral molecules at the colloidal and the aqueous interfaces*; COLUMBIA UNIVERSITY, 2009.
(39) Datta, C.; Naidu, R.; Yenkie, M. Photo-oxidative degradation of synthetic organic pollutant p-nitrophenol. *Journal of Scientific and Industrial Research* **2004**, *63*, 518-521.
(40) Bing, C.; Chun, Y.; Khang, G. Direct photolysis of nitroaromatic compounds in aqueous solutions. *Journal of Environmental Science (China)* **2005**, *17*, 598-604.
(41) Svetlichnyi, V.; Chaikovskaya, O.; Kuznetsova, R.; Sokolova, I.; Kopylova, T.; Meshalkin, Y. P. Photolysis of phenol and para-chlorophenol by UV laser excitation. *High Energy Chemistry* **2001**, *35*, 258-264.
(42) Alapi, T.; Dombi, A. Comparative study of the UV and UV/VUV-induced photolysis of phenol in aqueous solution. *Journal of Photochemistry and Photobiology A: Chemistry* **2007**, *188*, 409-418.
(43) Chun, H.; Yizhong, W.; Hongxiao, T. Destruction of phenol aqueous solution by photocatalysis or direct photolysis. *Chemosphere* **2000**, *41*, 1205-1209.
(44) Yu, J.; Zhang, P.; Yu, H.; Trapalis, C. Environmental photocatalysis. *International Journal of Photoenergy* **2012**, *2012*.
(45) Akbal, F.; Onar, A. N. Photocatalytic degradation of phenol. *Environmental monitoring and assessment* **2003**, *83*, 295-302.

(46) Zhao, S.; Ma, H.; Wang, M.; Cao, C.; Xiong, J.; Xu, Y.; Yao, S. Study on the mechanism of photo-degradation of p-nitrophenol exposed to 254nm UV light. *Journal of hazardous materials* **2010**, *180*, 86-90.
(47) Alif, A.; Boule, P.; Lemaire, J. Comportement photochimique du nitro-4 phenol en solution aqueuse. *Chemosphere* **1987**, *16*, 2213-2223.
(48) Zhao, S.; Ma, H.; Wang, M.; Cao, C.; Xiong, J.; Xu, Y.; Yao, S. Role of primary reaction initiated by 254 nm UV light in the degradation of p-nitrophenol attacked by hydroxyl radicals. *Photochemical & Photobiological Sciences* **2010**, *9*, 710-715.
(49) Machalický, O.; Lichý, L.; Bad'ura, J.; Hrdina, R.; Miranda, T. A kinetic description of monomolecular photochemical reaction with the use of polychromatic irradiation. *Journal of Photochemistry and Photobiology A: Chemistry* **2006**, *180*, 28-37.
(50) Nix, M.; Devine, A. L.; Cronin, B. d.; Dixon, R. N.; Ashfold, M. High resolution photofragment translational spectroscopy studies of the near ultraviolet photolysis of phenol. *The Journal of chemical physics* **2006**, *125*, 133318-133318.
(51) O'Neill, P.; Steenken, S.; van der Linde, H.; Schulte-Frohlinde, D. Reaction of OH radicals with nitrophenols in aqueous solution. *Radiation Physics and Chemistry (1977)* **1978**, *12*, 13-17.
(52) Suarez, C.; Louys, F.; Günther, K.; Eiben, K. OH-radical induced denitration of nitrophenols. *Tetrahedron Letters* **1970**, *11*, 575-578.

Chapter 2: Experimental

2.1 Surface SHG

A solid state Nd:YVO_4 laser (Spectra-Physics, Millennia PRO 15sJ) was used to pump a Ti:Sapphire Tsunami oscillator (Spectra-Physics, 3941X1BB) generating 70 fs pulses at 80 MHz. The Tsunami was tuned to produce an 800 nm fundamental beam, which was directed toward a Teflon dish containing 50 mL of the sample to be tested (Fig. 2-1). Prior to impinging upon the surface, the beam passed through a neutral density filter to reduce the incident power so as to prevent any thermal effects or burning of the sample. A polarizer and a half-wave plate were included to select and then modulate the linear polarization of light. Both the polarizer and half-wave plate were calibrated in the experimental geometry and installed with respect to the surface normal such that p-polarized light (0°) is parallel to the surface normal whereas s-polarized light (90°) is perpendicular. The light was then passed through a longpass filter to remove any 400 nm light that could be present in this geometry. A lens then focused the beam onto the surface at a 70° angle of incidence, which relates to the determination of SHG orientational fitting coefficients

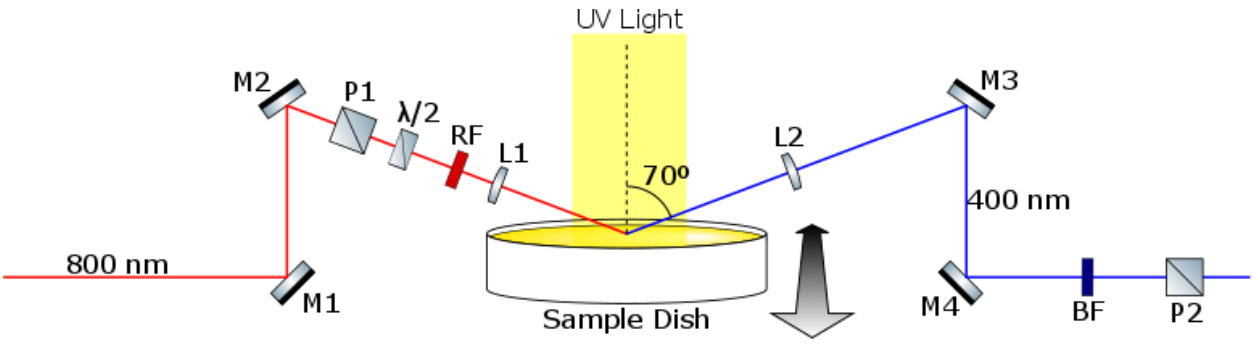

Figure 2-1: Optical schematic for the surface SHG experiments. The 800 nm fundamental beam is incident upon the surface, generating a 400 nm SH signal. The UV light is only used during the surface photochemistry experiments. The arrow picutred here represents translation into and out of the page. [M=mirror, P=polarizer, λ/2=half-wave plate, RF=red (longpass) filter, L=Lens, BF=blue (shortpass) filter]

(Appendix-I). The 800 nm fundamental beam generated the SH signal upon interaction with the solution surface and was reflected. After reflecting off the surface, the SH beam was then collimated and passed through a shortpass filter, removing any remaining 800 nm light. A polarizer was then used to select the polarization of light to be analyzed. The intensity of the SH signal, I_{SHG}, was focused into a monochromator (Acton SP2500, Princeton Instruments) for detection by a PMT camera (H11461P-01, Hamamatsu). This optical setup was confirmed to provide a strong SH response from a silver reference mirror (Appendix-II). The photocurrent from the PMT was fed into a 350 MHz preamplifier (SR445A, Stanford Research Systems, Inc.) with three 50 Ω channels cascaded for a gain of 125x. The preamplifier and alignment was optimized using a silver reference mirror (Appendix-II). The amplified signal was then sent to a single photon counter (SR400, Stanford Research Systems, Inc.) to be analyzed and then processed by LabView Software. The signal generated at the air-water interface was confirmed to be the SH by adjusting the power incident on the sample (Appendix-III). During each surface SHG experiment, the power incident on the sample was measured before each data collection period to ensure that the laser power remained stable. Optical components were purchased from Thor Labs and Newport Corporation.

2.1.1 Solution Preparation

Unless specifically stated, all compounds were purchased from Sigma Aldrich and used as received. Stock pH 2 and pH 13 solutions were prepared by dissolving concentrated HCl (ACS Reagent, 37%, 320331-500ML) or solid NaOH (ACS reagent, ≥97.0%, 221465-500G) in deionized (Millipore, Milli-Q 18.2 MΩ cm^{-1}). The pH was measured using a pH meter (AB150, Fischer Scientific) that was calibrated immediately prior to use. Solid PNP (Reagent Grade, ≥ 99%, 241326-50G) was dissolved in the pH 2 or pH 13 stock to yield 500 mL of 70 mM PNP and

130 mM PNP^- respectively. The pH of the resulting solutions was tested and showed little deviation from the pH of the stock solutions. The PNP and PNP^- solutions were then diluted using the appropriate stock pH 2 or pH 13 solution in order to obtain a range of concentrations. Millipore water and pH solutions were used as references. For each sample and reference, 50 mL of solution was added to a 6.5 cm diameter Teflon dish and given 15-20 minutes for the surface to equilibrate. All glassware and the Teflon dish were soaked in *aqua regia* for 15-30 minutes and then rinsed with copious amounts of distilled and Millipore water prior to use. The dish was then carefully moved into the experimental geometry on a motorized translation stage (MT S50-Z8). In order to prevent any thermal effects and control for any variation in the non-planarity of the surface, the translation stage was set to oscillate a distance of 7 mm in a direction perpendicular to both the surface normal and the direction of the laser propagation vector. The stage oscillated at a velocity no greater than 0.2 mm/s to prevent any perturbation of the surface.

2.1.2 Surface Equilibrium

The signal arising from the surface SHG was optimized by raising or lowering the height of the translation stage at a polarization configuration of p-in, p-out. Three spectra from 380 to 420 nm were then collected from the sample and the wavelength corresponding to the signal maximum (~400 nm) was set as the wavelength at which subsequent measurements were taken. The half-wave plate was then rotated with a motor to collect three data points for every 4.5° and was rotated a total of 180°, corresponding to a modulation of the light such that polarization data was collected every 9° over 360° of rotation for PNP. A similar procedure was used for PNP^-, but five data points were taken for every 3° of rotation of the half-wave plate. The output analyzer was then manually

rotated from p-out to s-out and data was collected by rotating the input polarizer as described above.

2.1.3 Surface Spectrum of PNP^-

The fundamental beam generated by the Ti:Sapphire laser was tuned to various wavelengths. At each wavelength, three spectra were collected such that the SH peak could be observed. This procedure was carried out in the same geometry as described above for three different samples; a Z-cut quartz reference crystal that was affixed to a Teflon dish and placed in the geometry without translation, a sample of pH 13 solution and a sample of 130 mM PNP^-.

2.2 Irradiation by Polychromatic UV Light

Photolysis was carried out by irradiating the samples with UV light generated by an ozone free 300 W Xenon arc Lamp (6258, Newport) installed in a research arc lamp housing with an F/1 type condenser lens and rear reflector (67005, Newport) which was connected to a power supply (69911, Newport). The light from the lamp was passed through an aluminum body liquid filter (67015, Newport) to remove IR radiation and then focused down onto either a 1 cm quartz cuvette in a Flash 300 temperature controlled cuvette holder or the Teflon dish. The incident power at both photodegradation sites was 0.4 W ca.. The light struck the cuvette through a 1 cm^2 window and the radius of the UV light incident on the Teflon dish was 2.5 cm.

2.2.1 Chemical Actinometry

Potassium ferrioxalate was selected as a chemical actinometer to determine the incident photon flux on the cuvette due to its sensitivity to irradiation by a wide range of wavelengths.[1,2] When excited by a photon, the ferrioxalate ion degrades into ferrous ions according to the following reaction (Eq. 2-1 & 2-2):

$$[Fe(C_2O_4)]^{-3} \xrightarrow{h\nu} Fe^{2+} + C_2O_4^{\cdot -} + 2C_2O_4^{2-} \quad \text{(Eq. 2-1)}$$

$$[Fe(C_2O_4)]^{-3} + C_2O_4^{\cdot -} \xrightarrow{\Delta} Fe^{2+} + 2CO_2 + 3C_2O_4^{2-} \quad \text{(Eq. 2-2)}$$

The ferrous ions produced can then form a complex with *o*-phenanthroline, resulting in a deep red color. A micro-version of the original procedure proposed by Hatchard and Parker was used for our determination.[1-4] Two solutions were prepared:

a) 250 mL of a 0.006 M potassium ferrioxalate was prepared from 0.75 g of solid potassium ferrioxalate trihydrate (31124, Alfa Aesar) dissolved in 0.05 M H_2SO_4 (diluted from ACS Reagent, 95.0-98.0% H_2SO_4).

b) 0.1% phenanthroline buffer was produced by dissolving 0.1 g of solid 1,10-phenanthroline monohydrate (ACS Reagent, T170-02, J.T. Baker) and 13.5 g of sodium acetate (ACS Reagent, ≥99.0%, 2411245-100G) in 100 mL of 0.5 M H_2SO_4.

All solutions were prepared under red light in glassware cleaned with *aqua regia* and rinsed with copious amounts of distilled and Millipore water.

The actinometry was carried out under red light as follows. 3 mL of solution (a) was placed into two 1 cm quartz cuvettes. One cuvette was left in the dark and the other was placed into the cuvette holder and held at 22°C with stirring. The sample in the cuvette holder was then irradiated. The irradiation time was measured by a stopwatch and recorded. 0.5 mL of solution (b) was then added to each cuvette and both cuvettes were stirred. UV/Vis spectra were then collected for the irradiated sample as well as the control and the difference in absorbance at 510 nm, corresponding to formation of the *o*-phenanthroline complex, was determined. The UV lamp power was such that the reaction progressed too quickly and neutral density filters were placed in the geometry to lower the incident power of the UV light onto the sample. The actinometry was performed at 3 second time intervals for three different combinations of neutral density filters until the conversion rate was no longer linear, which it is assumed to be early in the reaction. To correct for the difference

in power, the power of the UV light incident on the sample was measured for each combination and the absorbance of each neutral density filter was collected at two different positions on the filter and averaged.

A standard curve was generated by preparing a solution of 0.1 M $FeSO_4$ and 0.05 M H_2SO_4 and diluting that solution down to 400 mM $FeSO_4$ using more 0.05 M H_2SO_4. Ten different solutions were then prepared by addition of 0.0 to 1.0 mL in 0.1 mL increments of the 400 mM $FeSO_4$ solution. Further volumes of 0.05 M H_2SO_4 were added such that the volume of $FeSO_4$ and H_2SO_4 solutions was 2.0 mL. This was followed by addition of 1.4 mL of solution (b) and 0.6 mL of 0.05 M H_2SO_4. The UV/Vis spectrum of each solution was collected using the solution containing 0.0 mL of the $FeSO_4$ solution as a blank. Absorbance at 510 nm was plotted as a function of concentration and a molar extinction coefficient of $11290 \pm 20\ dm^3\ mol^{-1}\ cm^{-1}$ was calculated (Appendix-IV), which is in good agreement with literature values.[1-3]

2.2.2 Bulk Photochemistry

Solutions of PNP and PNP^- were prepared in the same manner as described for the SHG experiments and diluted into a range of concentrations so that the absorbance peaks could be detected with an Agilent Cary 8453 diode array UV/Vis Spectrometer. The molar extinction coefficients were determined to be $19350 \pm 50\ dm^3\ mol^{-1}\ cm^{-1}$ at 316 nm and $19420 \pm 70\ dm^3\ mol^{-1}\ cm^{-1}$ at 401 nm respectively (Appendix-V). Solutions of 109 μM of PNP and 129 μM PNP^- were prepared for photolysis. For each sample, approximately 4 mL of solution was placed into two 1 cm quartz cuvettes that were then capped to prevent evaporation. One cuvette was stored in the dark as a control and the other was placed into a Flash 300 temperature controlled cuvette holder and stirred at a constant temperature of 22°C. The sample in the cuvette holder was irradiated by UV light. Irradiation times measured by a stopwatch were recorded, and UV/Vis

spectra of both the irradiated sample and the control were collected. This procedure was performed on the same samples over a period of months and the samples were stored in the dark between experiments.

2.2.3 Surface Photochemistry

SHG data was collected using the same procedure as described above for the surface equilibrium but on a single sample of 130 mM PNP^{-}. The control for this experiment was left exposed to the room conditions and data was collected over time, which was measured by a stopwatch. Another sample was then prepared and irradiated by light from the UV lamp that had been redirected onto the center of the Teflon dish. In order to remove excess UV radiation that would otherwise affect our results, a box was constructed from foamboard to block the light which fit over the lamp housing during the times when data was being collected. During the surface photodegradation, the shutter for the monochromator was closed in order to prevent any damage to the cameras that may have been incurred from exposure to the UV light.

References

(1) Calvert, J. G.; Pitts, J. N. Photochemistry. **1966**.
(2) Montalti, M.; Credi, A.; Prodi, L.; Gandolfi, M. T.: *Handbook of photochemistry*; CRC press, 2006.
(3) Aillet, T.; Loubiere, K.; Dechy-Cabaret, O.; Prat, L. Accurate measurement of the photon flux received inside two continuous flow microphotoreactors by actinometry. *International Journal of Chemical Reactor Engineering* **2014**, *12*, 257-269.
(4) Bing, C.; Chun, Y.; Khang, G. Direct photolysis of nitroaromatic compounds in aqueous solutions. *Journal of Environmental Science (China)* **2005**, *17*, 598-604.

Chapter 3: Surface Equilibrium Properties of PNP and PNP^-

An important goal in this research project is to develop an understanding of the photochemistry of PNP and PNP^- adsorbed to the air-aqueous interface. Consequently, it is necessary to understand their surface equilibrium behavior with respect to average molecular orientation, affinity to the air-aqueous interface, other factors that may influence their adsorption to the surface, and any changes to the molecule that may occur at the interface. This chapter details the analytical methods used to determine these surface phenomena.

3.1 Average Molecular Orientations of the Molecules

SH intensity generated at the air-liquid interface was measured by rotating the input polarization of light, γ, at a constant output polarization, Γ, of either s- ($\Gamma = 90°$) or p- ($\Gamma = 0°$) polarized light. This procedure is carried out on solutions that represent a range of concentrations of both PNP and PNP^-. Data collected from each concentration may be fitted using Eq. 3-1, which assumes that the x- and y-axes are interchangeable and that the orientation of adsorbed molecules with respect to the surface normal is invariant with rotation about the z-axis,[1-7] applicable in the case of the air-aqueous interface. In the equation, $I_{2\omega}$ is the intensity of the second harmonic signal, γ and Γ are the input and output polarizations of light, respectively, such that p- is 0° and s- is 90°. The orientational fitting parameters, a_i, are coefficients relating to the fractions of reflected and refracted light upon interaction with the surface, and the $\chi^{(2)}$ terms are elements of the second order susceptibility. By holding the output polarization constant, at either s- or p-, this equation can be simplified (Eq. 3-2 & 3-3).

$$I_{2\omega} \propto \left| a_1 \chi^{(2)}_{XXZ} \sin(2\gamma)\sin(\Gamma) + \left(a_2 \chi^{(2)}_{XXZ} + a_3 \chi^{(2)}_{ZXX} + a_4 \chi^{(2)}_{ZZZ}\right)\cos^2(\gamma)\cos(\Gamma) + a_5 \chi^{(2)}_{ZXX} \sin^2(\gamma)\cos(\Gamma) \right|^2 \quad \text{(Eq. 3-1)}$$

$$I_{2\omega,s} \propto \left| a_1 \chi^{(2)}_{XXZ} \sin(2\gamma) \right|^2 \quad \text{(Eq. 3-2)}$$

$$I_{2\omega,p} \propto \left| \left(a_2 \chi^{(2)}_{XXZ} + a_3 \chi^{(2)}_{ZXX} + a_4 \chi^{(2)}_{ZZZ}\right)\cos^2(\gamma) + a_5 \chi^{(2)}_{ZXX} \sin^2(\gamma) \right|^2 \quad \text{(Eq. 3-3)}$$

In determining the molecular orientation of molecules at the surface, we used a nonlinear polarization sheet model of the surface to calculate the a_i coefficients (Appendix-I).

Fitting the data with this equation first required that we correct the collected SH intensity, $I_{SHG,raw}$, to remove any solvent contributions, $I_{SHG,solvent}$. SH intensity as a function of the input polarization angle was collected on a sample of pH 2 solution and pH 13 solution for experiments on PNP and PNP^-, respectively. The correction used is dependent on whether the molecule has a transition that is resonant with the laser, either at 400 nm or 800 nm, or if its transitions are nonresonant at these wavelengths. The absorbance spectra of PNP and PNP^- (Fig. 3-1) indicate

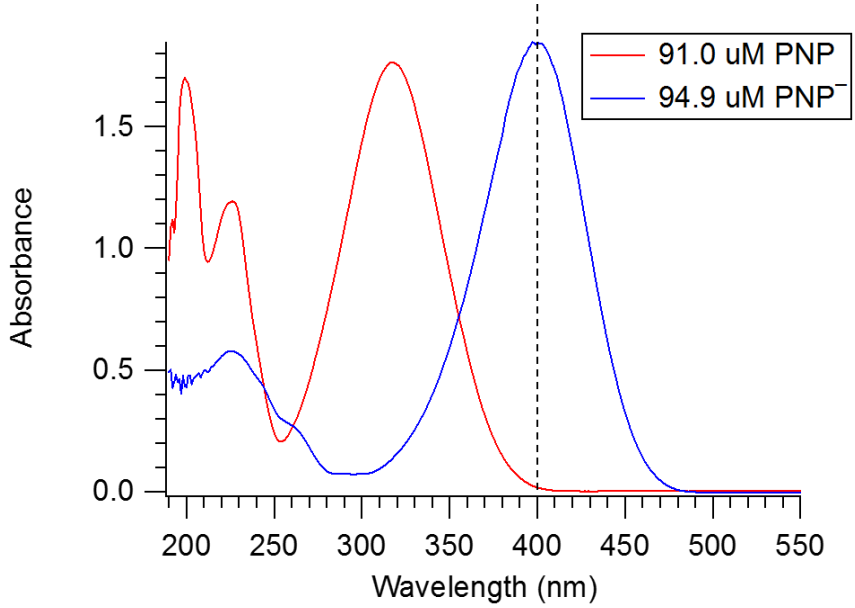

Figure 3-1: Absorbance spectra of a 91.0 µM solution of PNP in pH 2 solution (red line) and a 94.9 µM solution of PNP^- in pH 13 solution. The wavelength of SH signal is 400 nm (dashed line). Overlap with the absorbance peak of PNP^- provides resonant enhancement to the SH signal generated at the surface. PNP, however, is shown to be off-resonant, which results in a weak signal.

that PNP must be treated as nonresonant (Eq. 3-4), however, PNP^- can be treated as a resonant molecule (Eq. 3-5), which explains why the SH signals arising the surface of PNP^- solutions are much stronger than the signals obtained from PNP.

$$I_{SHG,PNP} = \left|\sqrt{I_{SHG,raw}} - \sqrt{I_{SHG,solvent}}\right|^2 \quad \text{(Eq. 3-4)}$$

$$I_{SHG,PNP^-} = I_{SHG,raw} - I_{SHG,solvent} \quad \text{(Eq. 3-5)}$$

After correction, I_{SHG} was plotted as a function of the input polarization angle (Fig. 3-2) for a single output polarization. The plot corresponding to s-output was then fit with Eq. 3-2 to yield the $\chi^{(2)}_{XXZ}$ susceptibility term, the only element upon which the SH intensity depends for the s-polarized output configuration. Subsequently, the plot of the p-out configuration was fit with Eq. 3-3, holding the value of $\chi^{(2)}_{XXZ}$ constant in order to obtain the $\chi^{(2)}_{ZXX}$ and $\chi^{(2)}_{ZZZ}$ terms.

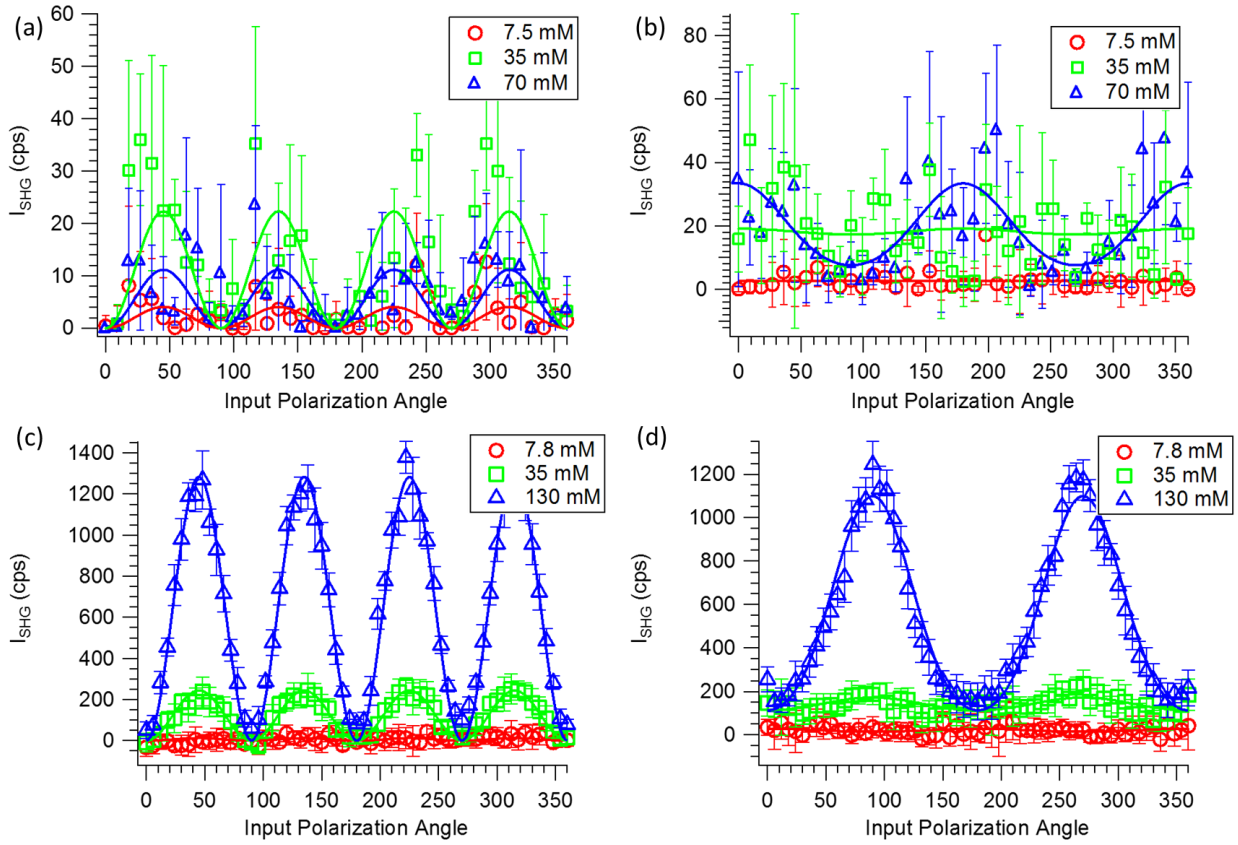

Figure 3-2: I_{SHG} plotted as a function of the input polarization angle, γ, and the fit lines produced from Eq. 3-2 & 3-3. Graphs (a) and (b) are the plots for s- and p-output, respectively, for PNP and graphs (c) and (d) are the plots for s- and p-output for PNP^-. The comparatively large magnitude of error in graph (a) and (b) can be attributed to instrument noise and the low intensities are due to the fact that PNP is nonresonant with both the fundamental and SH frequencies.

Once the $\chi^{(2)}$ terms have been determined, the SHG orientation parameter, D, can be calculated (Eq. 3-6), from an assumption that PNP and PNP^- are treated as rod-like molecules with a dominant β_{zzz} hyperpolarizability element.[4,7] Assuming that the distribution of the average molecular orientation is narrow, D is approximated as equal to a cosine squared function of $\langle\theta\rangle$, the average angle between the molecular axis and the surface normal (Eq. 3-7). For both PNP and PNP^-, we treat the molecular axis as consistent with the O–C bond of the molecule.

$$D \equiv \frac{\langle \cos^3\theta \rangle}{\langle \cos\theta \rangle} = \frac{\chi_{zzz}}{\chi_{zzz} + 2\chi_{zxx}} \quad \text{(Eq. 3-6)}$$

$$D \approx \cos^2\langle\theta\rangle \quad \text{(Eq. 3-7)}$$

Pictured below are plots of the average molecular orientation as a function of concentration (Fig. 3-3). In the case of PNP, the adsorbed molecules appear to tilt from the surface normal at an angle of around 44°, varying between 37° and 47°, however the orientational change does not appear to follow a discernable trend, therefore, it is reasonable to assume that the molecular orientation is remaining constant within the magnitude of the experimental uncertainty. The concentration dependent orientational profile of PNP^-, however, behaves much differently. As the bulk concentration of the solution increases, corresponding to an increase in the surface number

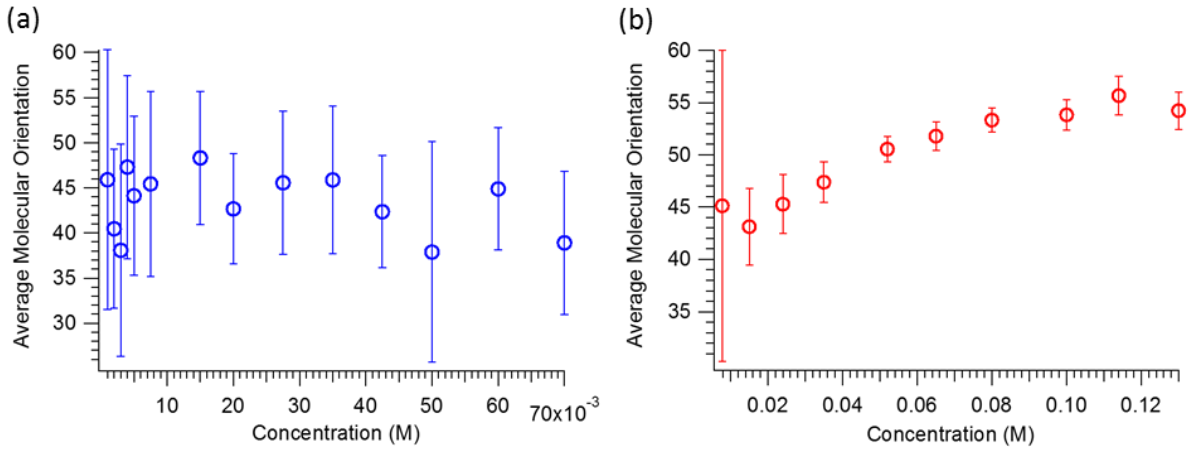

Figure 3-3: The graphs pictured here illustrate the reorientation about the surface normal that PNP (a) and PNP^- (b) undergo as a function of the surface number density. Within the error bar, the tilt angle of PNP remains relatively constant, but as the number of ions present at the surface increases, PNP^- begins to conform to a configuration that is nearer to the interface.

density, the tilt angle between the molecular axis and the surface normal increases from a value of approximately 43° to 54°. The physical representation of this trend is that as number density of PNP^- anions at the surface increases, the anions begin to settle into a configuration that moves the partial negative charge on the nitro group closer the plane of the surface.

3.2 Surface Affinity Determination

Utilizing the same data collected for the average molecular orientation determinations, we can determine the affinity of the molecules to the surface. Since the SH field is proportional to the second-order susceptibility term, it is thereby proportional to the number of molecules adsorbed to the surface and their orientation (Eq. 3-8).[6,8-14] From this relation, we may plot $\vec{E}_{SHG}$, calculated from the corrected intensities (Eq. 3-9), collected from a single polarization configuration as a function of bulk concentration, C, corrected for water by dividing by 55.5. The data is then fit with a Langmuir isotherm model (Eq. 3-10), commonly used to determine adsorption affinities to the air-water interface using SHG,[3,8,10,11,14-16] this isotherm model assumes monolayer coverage on surfaces that are planar and homogeneous, and that the adsorbates do not interact with one another. From the fitting parameter, K_{ads}, we then calculate the Gibbs free energy adsorption, ΔG_{ads} (Eq. 3-11).

$$\vec{E}_{SHG} \propto \chi^{(2)} \propto N_s\langle\beta^{(2)}\rangle \quad \text{(Eq. 3-8)}$$

$$\vec{E}_{SHG} = \sqrt{I_{SHG}} \quad \text{(Eq. 3-9)}$$

$$\frac{N_s}{N_{max}} = \frac{K_{ads}C}{1 + K_{ads}C} \quad \text{(Eq. 3-10)}$$

$$\Delta G_{ads} = -RTln(K_{ads}) \quad \text{(Eq. 3-11)}$$

Fig. 3-4 and 3-5 show adsorption isotherms of PNP and PNP^-, respectively, for four distinct polarization configurations: p-in p-out (a), s-in p-out (b), 45°-in p-out (c), and 45°-in s-out (d). In the case of PNP (Fig. 3-4), the value of ΔG_{ads} remained constant for each configuration, yielding an average ΔG_{ads} of -22 ± 2 kJ mol^{-1}. In contrast, the fit for PNP^- (Fig. 3-5) returned adsorption free energies of between -15.1 ± 0.3 kJ mol^{-1} to -21.2 ± 0.8 kJ mol^{-1}. Since the equilibrium constant only relates to the relative number of molecules adsorbed to the surface and $\vec{E}_{SHG}$ relates to both the number of adsorbed molecules and their average molecular orientation, fitting the data

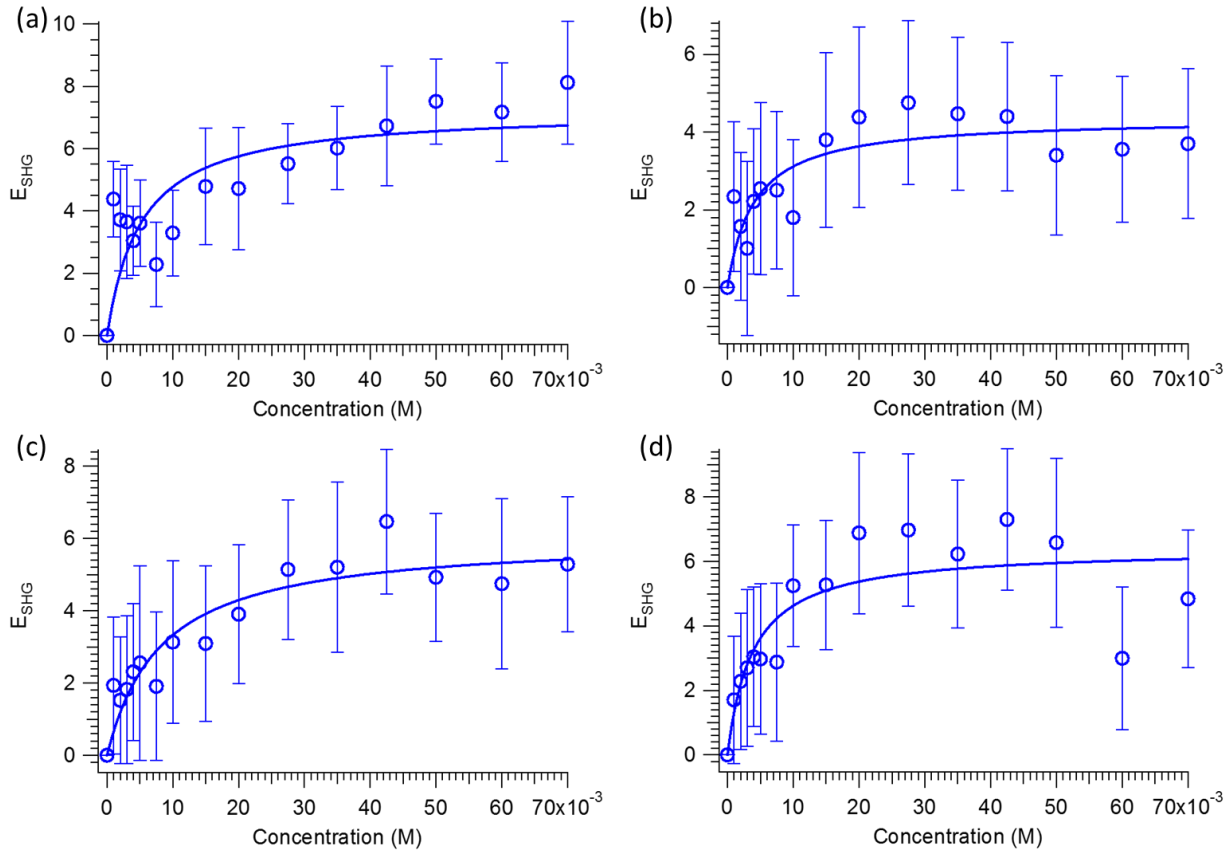

Figure 3-4: PNP adsorption isotherms fit with the Langmuir isotherm model at four different polarization configurations, p-in p-out (a), s-in p-out (b), 45°-in p-out (c), and 45°-in s-out (d). The value of ΔG_{ads} at each configuration was relatively invariant, with (a), (b), and (d) resulting in -23 ± 1 $kJ\ mol^{-1}$ and (c) returning a value of -21.6 ± 1 $kJ\ mol^{-1}$.

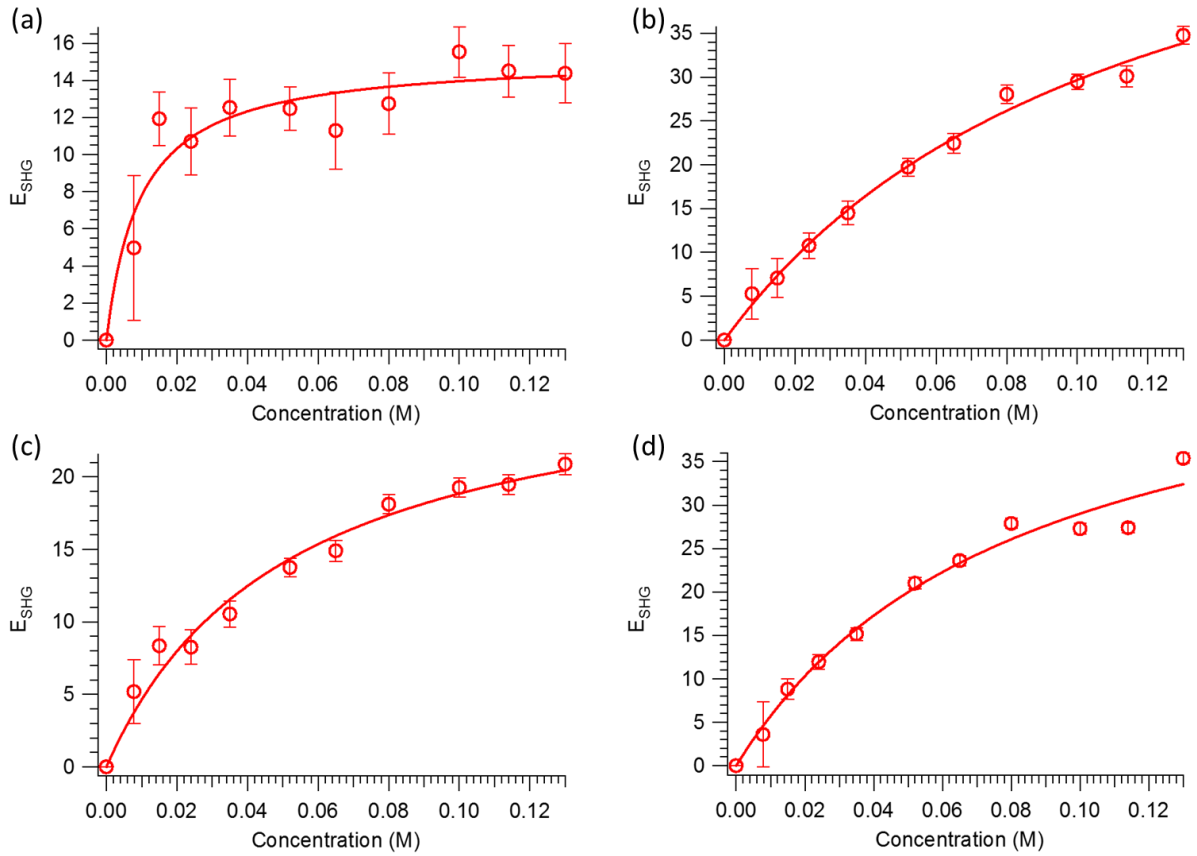

Figure 3-5: PNP^- adsorption isotherms fit with the Langmuir isotherm model at four different polarization configurations, p-in p-out (a), s-in p-out (b), 45°-in p-out (c), and 45°-in s-out (d). The value of ΔG_{ads} at each configuration varied, with values of $-21.2 \pm 0.8\ kJ\ mol^{-1}$ (a), $-15.1 \pm 0.3\ kJ\ mol^{-1}$ (b), $-17.1 \pm 0.4\ kJ\ mol^{-1}$ (c), and $-16.0 \pm 0.06\ kJ\ mol^{-1}$ (d).

with the Langmuir isotherm is only applicable if the average molecular orientation of the adsorbed molecules is constant over a range of concentrations. A more appropriate polarization configuration, one where the SH field does not vary much as the orientation of the molecules change, needs to be used. This orientation insensitive angle, γ^*, for the p-output configuration is calculated from the same a_i coefficients (Appendix-I) as were used previously in the determination of the molecular orientation (Eq. 3-12).[7,16,17]

$$\gamma^* = \cos^{-1}\left(\frac{a_5}{3a_4 + a_5 - a_2 - a_3}\right) \qquad \text{(Eq. 3-12)}$$

In our geometry, the orientation insensitive angle was found to be 61.5°. Fitting the isotherms obtained from this approximate configuration (Fig. 3-6), 63° for PNP and 60° for PNP^- due to the experimental parameters set, yielded ΔG_{ads} values of $-24.7 \pm 0.6\,\mathrm{kJ\,mol^{-1}}$ and $-16.0 \pm 0.3\,\mathrm{kJ\,mol^{-1}}$, respectively. The relative invariance of ΔG_{ads} at each polarization configuration gives us added confidence in our results from the molecular orientation determination, in that the orientation of PNP does not vary with changing surface number density, but PNP^- does.

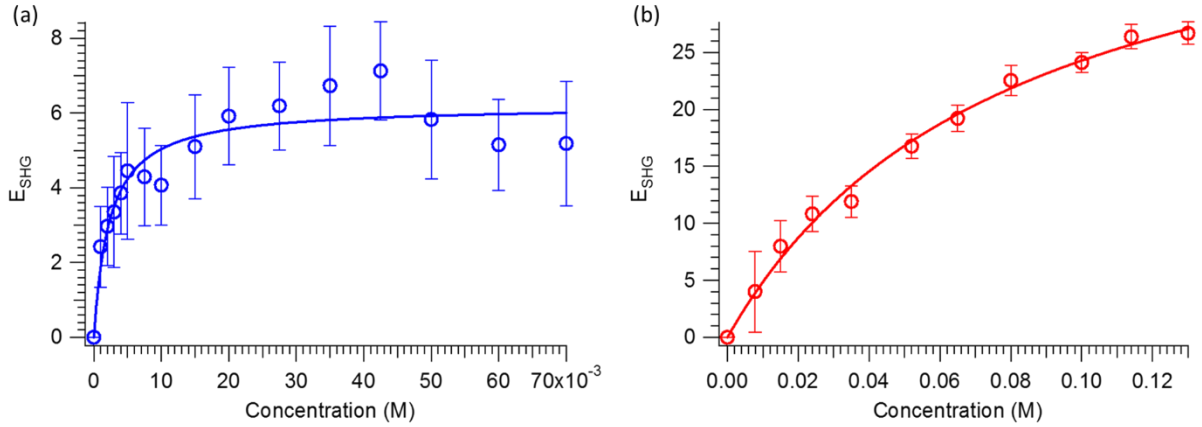

Figure 3-6: Langmuir adsorption isotherms of PNP (a) and PNP- (b) collected at the orientation insensitive polarization configuration resulting in ΔG_{ads} values of $-24.7 \pm 0.6\ kJ\ mol^{-1}$ and $-16.0 \pm 0.3\ kJ\ mol^{-1}$, respectively.

3.3 Surface SHG Spectrum of PNP^-

The three spectra collected from PNP^- were averaged and the SH intensity at the peak of each averaged spectrum was extracted and plotted as a function of wavelength (Fig. 3-7(a)). This plot represents the raw SHG spectrum of PNP^- adsorbed to the air-water interface. The raw SHG

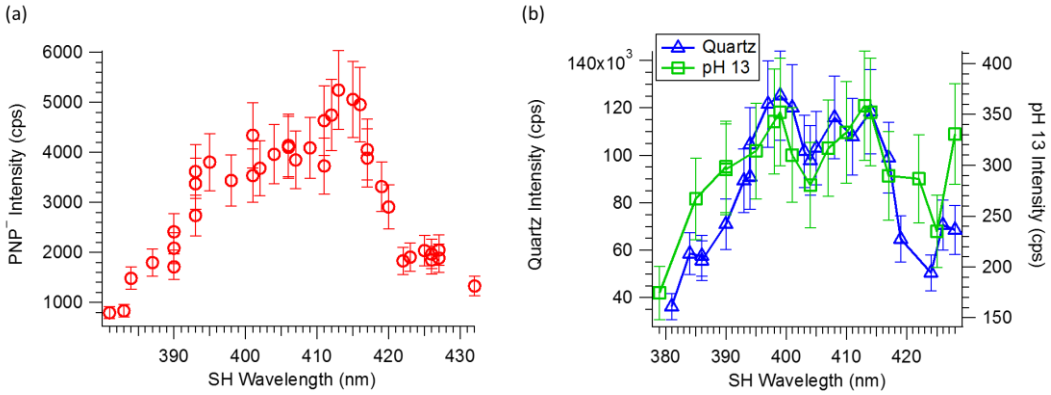

Figure 3-7: Raw surface SH spectra of PNP^- (a), quartz (b), and pH 13 (b) samples. The raw spectrum of PNP^- is reflective of the molecular transition of the molecule, optical throughput of the setup used, and wavelength dependent changes laser power. Since neither the quartz nor pH 13 samples have molecular transitions near the fundamental or SH frequency, the features in their spectra are attributed solely to the optical throughput and laser power variations.

spectra of the quartz crystal and pH 13 solutions were collected as references (Fig. 3-7(b)), and since they do not have an electronic transition in this range, the features of their plots are reflective of variations in the intensity of the SH signal that arise from tuning the laser. As in the previous two sections, the raw SH intensity of the pH 13 solution was subtracted from the PNP^- to correct for the solvent contribution. The solvent corrected SH intensities were then normalized with the pH 13 spectrum. Using the pH 13 spectrum as opposed to the quartz spectrum was preferable since the SH signal from pH 13 was weaker and therefore less sensitive to changes which may arise from variations in the room environment.

The resulting spectrum (Fig. 3-8) is a representation of the electronic transition of PNP^- at the surface. Comparing the surface SHG spectrum to the absorption spectrum of PNP^- in bulk solution reveals that the excitation wavelength differs at the surface. The absorption spectrum of bulk PNP^- has a spectroscopy peak at 400 nm, however, this peak shifts to 408 nm upon adsorption

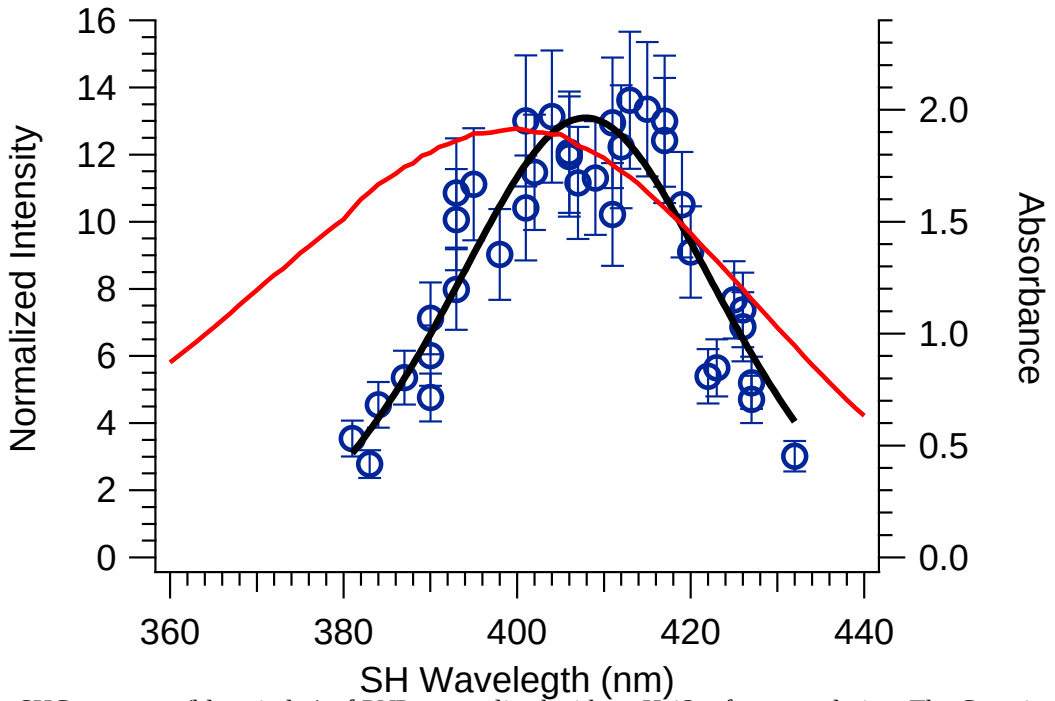

Figure 3-8: SHG spectrum (blue circles) of PNP^- normalized with a pH 13 reference solution. The Gaussian fit line (black line) shows that surface spectrum peaks at 408 nm. An 8 nm red shift from the absorbance peak (red line) at 400 nm is observed. This shift in the excitation frequency suggests that the molecule is experiencing a change at the surface that brings the ground, S_0, and excited, S_1, states closer together.

to the air-water interface. This shift is indicative of changes in its molecular structure or chemical environment such that the ground state of the molecule, S_0, is destabilized, the excited state, S_1, has been stabilized, or that the molecular transition is affected by Franck-Condon factors when adsorbed to the surface.

References

(1) Brevet, P. F.; Girault, H. H. Second harmonic generation at liquid/liquid interfaces. *Liquid-Liquid Interfaces: Theory and Methods. AG Volkov and DW Deamer, editors. CRC Press, Boca Raton, FL* **1996**, 103-137.

(2) Corn, R. M.; Higgins, D. A. Optical second harmonic generation as a probe of surface chemistry. *Chemical reviews* **1994**, *94*, 107-125.

(3) Higgins, D. A.; Abrams, M. B.; Byerly, S. K.; Corn, R. M. Resonant second harmonic generation studies of p-nitrophenol adsorption at condensed-phase interfaces. *Langmuir* **1992**, *8*, 1994-2000.

(4) Simpson, G. J.; Westerbuhr, S. G.; Rowlen, K. L. Molecular orientation and angular distribution probed by angle-resolved absorbance and second harmonic generation. *Analytical chemistry* **2000**, *72*, 887-898.

(5) TamburelloáLuca, A. A. Surface second-harmonic generation at air/solvent and solvent/solvent interfaces. *Journal of the Chemical Society, Faraday Transactions* **1995**, *91*, 1763-1768.

(6) Tamburello-Luca, A. A.; Hebert, P.; Brevet, P. F.; Girault, H. H. Resonant-surface second-harmonic generation studies of phenol derivatives at air/water and hexane/water interfaces. *J. Chem. Soc., Faraday Trans.* **1996**, *92*, 3079-3085.

(7) Simpson, G. J.; Rowlen, K. L. Orientation-insensitive methodology for second harmonic generation. 1. Theory. *Analytical chemistry* **2000**, *72*, 3399-3406.

(8) Bhattacharyya, K.; Castro, A.; Sitzmann, E.; Eisenthal, K. Studies of neutral and charged molecules at the air/water interface by surface second harmonic generation: Hydrophobic and solvation effects. *The Journal of chemical physics* **1988**, *89*, 3376-3377.

(9) Bhattacharyya, K.; Sitzmann, E.; Eisenthal, K. Study of chemical reactions by surface second harmonic generation: p-Nitrophenol at the air–water interface. *The Journal of chemical physics* **1987**, *87*, 1442-1443.

(10) Castro, A.; Bhattacharyya, K.; Eisenthal, K. B. Energetics of adsorption of neutral and charged molecules at the air/water interface by second harmonic generation: Hydrophobic and solvation effects. *The Journal of chemical physics* **1991**, *95*, 1310-1315.

(11) Eisenthal, K. Liquid interfaces probed by second-harmonic and sum-frequency spectroscopy. *Chemical Reviews* **1996**, *96*, 1343-1360.

(12) Shen, Y. Surface properties probed by second-harmonic and sum-frequency generation. *Nature* **1989**, *337*, 519-525.

(13) Shen, Y.-R. Principles of nonlinear optics. **1984**.

(14) Woods, B. L.; Walker, R. A. pH effects on molecular adsorption and solvation of p-nitrophenol at silica/aqueous interfaces. *The Journal of Physical Chemistry A* **2013**, *117*, 6224-6233.

(15) Somorjai, G. A.: *Principles of surface chemistry*; Prentice-Hall: Englewood Cliffs, N.J, 1972.

(16) Simpson, G. J.; Rowlen, K. L. Orientation-insensitive methodology for second harmonic generation. 2. Application to adsorption isotherm and kinetics measurements. *Analytical chemistry* **2000**, *72*, 3407-3411.

(17) Simpson, G. J. New tools for surface second-harmonic generation. *Applied Spectroscopy* **2001**, *55*, 16A-16A.

Chapter 4: Photochemistry of PNP and PNP^-

The results obtained from the study of PNP and PNP^- adsorbed to the air-water interface represent the surface equilibrium properties of an unperturbed surface, which serve as a reference in the investigation of the surface photochemistry of PNP and PNP^-. An objective of the research project is to provide a quantitative comparison of the photodecomposition of PNP^- at the air-water interface to the same process occurring in bulk solution. Presented here is a discussion detailing the experimental quantification of the UV light source determined from potassium ferrioxalate actinometry, and a determination of the photolysis quantum efficiencies of PNP and PNP^-. Lastly, outcomes of a determination of the surface properties of PNP^- as it undergoes irradiation are presented and compared to the unperturbed surface as well as to the bulk photochemistry.

4.1 Chemical Actinometry

Calculations for the incident photon flux on our samples from a polychromatic light source were carried out in the manner described by Aillet *et al.*[1] Here, the rate of conversion of the actinometer, $\frac{dX}{dt}$, is expressed as a function of wavelength dependent parameters and experimental variables (Eq. 4-1 & 4-2).

$$\frac{dX}{dt} = \frac{q_{p,0}}{C_{A0}V_r}\sum\nolimits_{\Delta\lambda_i}(T_{\lambda_i}\Phi_{\lambda_i}g_{\lambda_i}f_{\lambda_i}) \qquad \text{(Eq. 4-1)}$$

In the equation, X is the conversion of the actinometer such that:

$$X = \frac{C_{Fe^{2+}}}{C_{A0}} \qquad \text{(Eq. 4-2)}$$

where $C_{Fe^{2+}}$ is the concentration of the ferrous ion produced by irradiating a sample of the potassium ferrioxalate solution of concentration, C_{A0}. In the equations above, V_r is the volume of

solution in the reaction vessel in mL and $q_{p,0}$ is the total incoming photon flux. The transmittance function, T_λ, and the density function, g_λ, are the material transmittance of the optical components and the relative number of photons emitted from the UV light source per second, respectively. The quantum yield, Φ_λ, refers to the number of products produced per photon, and f_λ is the fraction of light absorbed by the actinometer. Each wavelength dependent parameter must be determined for discrete wavelengths within the range, $\Delta\lambda$. In our calculations, we modeled values of the wavelength dependent variables in the range of 200 to 550 nm in 1 nm increments.

Values of g_λ were obtained nm by modeling spectral irradiance data for the lamp, applying correction factors for the condenser lens and rear reflector as provided by the supplier,[2,3] and converting to the number of moles of photons emitted per second relative to the total number of moles of photons per second at all wavelengths (Appendix-VI). The quantum yield of potassium ferrioxalate at each wavelength was approximated from a plot of the known literature values of the quantum yield[4-7] as a function of wavelength which was then fit to a fourth order polynomial, which produced a fit function similar in both magnitude and shape to the fourth order polynomial expression reported by Bing *et al.*[6] (Appendix-VII). The fraction of light absorbed by the actinometer was then calculated using Eq. 4-3:

$$f_{\lambda_i} = 1 - e^{-\kappa_{\lambda_i} C_{A0}(1-X)\ell} \qquad \text{(Eq. 4-3)}$$

where κ_{λ_i} is the Napierian molar absorption coefficient, which is derived from a Beer's Law relationship such that $A_\kappa = \kappa\ell c$, where c is the concentration in mol dm^{-3}, ℓ is the pathlength of the cell in cm, and A_κ is the log base e material absorbance. More commonly, Beer's law is expressed as $A = \varepsilon\ell c$, where ε is the molar extinction coefficient, and A is the log base 10 material absorbance. These terms differ only in the way they relate material absorbance to material transmittance, T, such that $A_\kappa = -\ln T$ and $A = -\log T$. The Napierian molar absorption

coefficient was also fit to an equation using known literature values[1] (Appendix-VIII). The transmittance function was determined experimentally from the UV/Vis spectrum of the neutral density filters installed in the path between the UV lamp and the cuvette. The absorbance spectrum of each filter was converted to a transmittance spectrum and the transmittance spectrum of the three neutral density filters used in concert were multiplied together to determine the net transmittance.

The sum of the products of the wavelength dependent parameters is constant for a single neutral density filter combination, as is the initial concentration of the actinometer solution, 0.006 M, and the volume of solution in the reaction vessel, 3.5 mL. It is important to note that the rate of conversion of the actinometer is approximately linear at less than 10% conversion, such that X was held constant at a value of zero in Eq. 4-3.

From the experiment, the concentration of ferrous ions in solution after the addition of 0.5 mL of the *o*-phenanthroline buffer is calculated from the change in absorbance at 510 nm, ΔA_{510}, and the extinction coefficient from the standard curve, ε_{510}, using the Beer-Lambert Law. Converting this concentration from the final volume, V_2, to the concentration of ferrous ions produced in the reaction vessel and dividing by the initial concentration of the actinometer returns the value of X (Eq. 4-4).

$$X = \frac{C_{Fe^{2+}}}{C_{A0}} = \frac{\Delta A_{510} V_2}{C_{A0} \varepsilon_{510} V_r} \qquad \text{(Eq. 4-4)}$$

Using nonlinear regression analysis, the incoming photon flux was determined by minimizing the RMSE in the values of X from each experiment performed with one of the neutral density filter combinations and from the model (Eq. 4-5).

$$RMSE = \sum_i \left[(X)^i_{model} - (X)^i_{experiment} \right]^2 \qquad \text{(Eq. 4-5)}$$

Each neutral density filter combination resulted in a $q_{p,0}$ of approximately 6×10^{-7} einstein s^{-1}. To determine the incoming photon flux for a configuration with no neutral density filters, we determined the rate of conversion with each neutral density filter combination (Fig. 4-1). We then

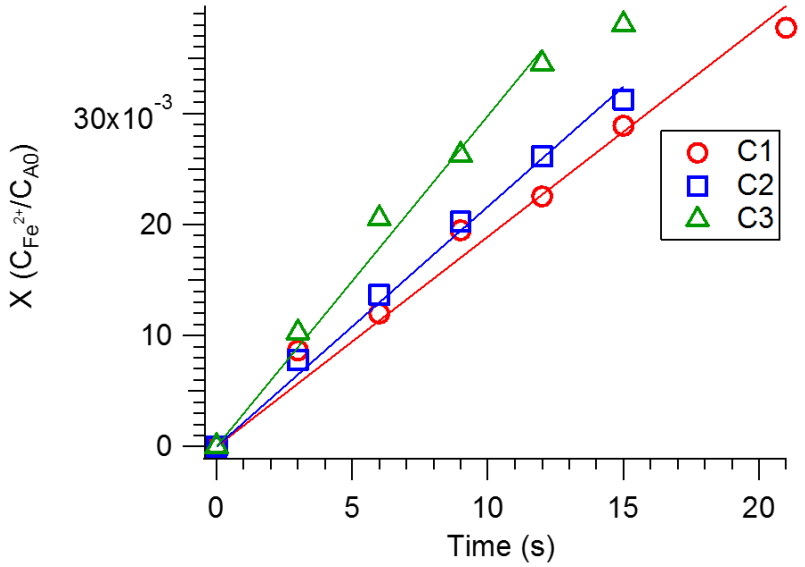

Figure 4-1: The conversion of the actinometer, X, plotted as a function of time allows us to determine the rate of conversion by fitting the data points with a line. Each line in the figure represents a specific neutral density filter combination (C1, C2, or C3) for which the slope was calculated.

assumed that the reaction rate would be linearly proportional to the UV lamp power incident upon the sample (Fig. 4-2). The reaction rate at an incident lamp power of 0.4 W was calculated from

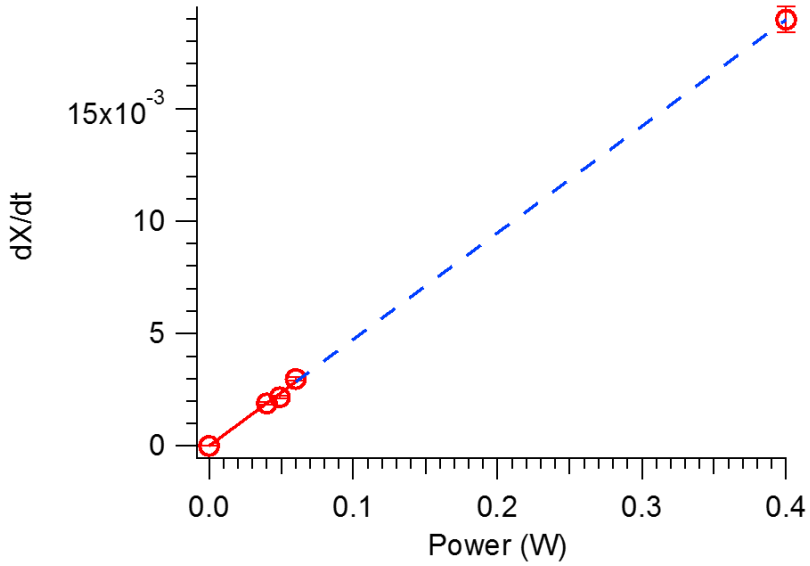

Figure 4-2: Plotting the conversion rate as a function of the incident power allows us to extrapolate the conversion rate of the actinometer at an incident UV lamp power consistent with a geometry without any neutral density filters.

the change in reaction rate with respect to incident power. This reaction rate was then substituted back into the Excel model and the transmittance function was set to 1 for all wavelengths, which assumes that the wavelength dependent absorption of the other optical components in the geometry was negligible. We report an incoming photon flux of $(6.3 \pm 0.2) \times 10^{-7}$ einstein s^{-1}. Error was propagated from the 95% CI of slope of the fit line in Fig. 4-2 as it is reflective of the major source of experimental error, which is error in the measurements of irradiation times.

	C1	**C2**	**C3**	**C0**
Incident Power (W)	0.04	0.049	0.06	0.4
$\frac{dX}{dt}$ $(s^{-1} \times 10^{-4})$	18.9 ± 0.6	21.6 ± 0.4	20 ± 1	190 ± 7

Table 4-1: Power of the UV lamp incident on the cuvette and conversion rates interpolated from the linear fit lines for each neutral density filter combination used. C0 in the table is in reference to the incident power and extrapolated conversion rate for an experimental setup with no neutral density filters.

From the incoming photon flux, we may then calculate the incident photon flux on our samples at discrete wavelengths using Eq. 4-6. Again, we assume that the transmittance of the optical components in our geometry is negligible such that $T_\lambda = 1$ for all wavelengths between 200 and 550 nm. Finally, the sum over all wavelengths in the range is the total photon flux received by the sample, $q_{p,\Delta\lambda}$, which can be calculated for any range of wavelengths that $q_{p,0}$ was calculated for (Eq. 4-7).

$$q_{p,\lambda} = T_\lambda g_\lambda q_{p,0} \quad \text{(Eq. 4-6)}$$

$$q_{p,\Delta\lambda} = \sum\nolimits_{\Delta\lambda_i} q_{p,\lambda_i} \quad \text{(Eq. 4-7)}$$

Finally, the total incident photon flux received by a sample undergoing photolysis can be used to calculate the quantum efficiency, $\varphi_{\Delta\lambda}$, of the molecule[6] (Eq. 4-8 & 4-9).

$$f_\lambda = 1 - 10^{-A_{\lambda,0}} \quad \text{(Eq. 4-8)}$$

$$\varphi_{\Delta\lambda} = r\frac{V}{\sum_{\Delta\lambda} f_\lambda q_{p,\lambda}} \quad \text{(Eq. 4-9)}$$

From these equations, the fraction of light absorbed by the molecule at a specific wavelength, f_λ,

is calculated from the absorbance spectrum of the sample collected before being irradiated, $A_{\lambda,0}$, such that the UV exposure time is 0 seconds. The quantum efficiency of the reaction is then calculated for the range specified by $\Delta\lambda$ where V is the irradiation volume and r is the reaction rate.

4.2 Bulk Photochemistry

The photolytic process in the bulk was determined from UV/Vis spectra collected at different irradiation times (Fig. 4-3). Absorbance measurements taken at 318 nm for PNP and 400 nm for PNP^- were recorded for both a photodegraded sample and a control. As the kinetics for

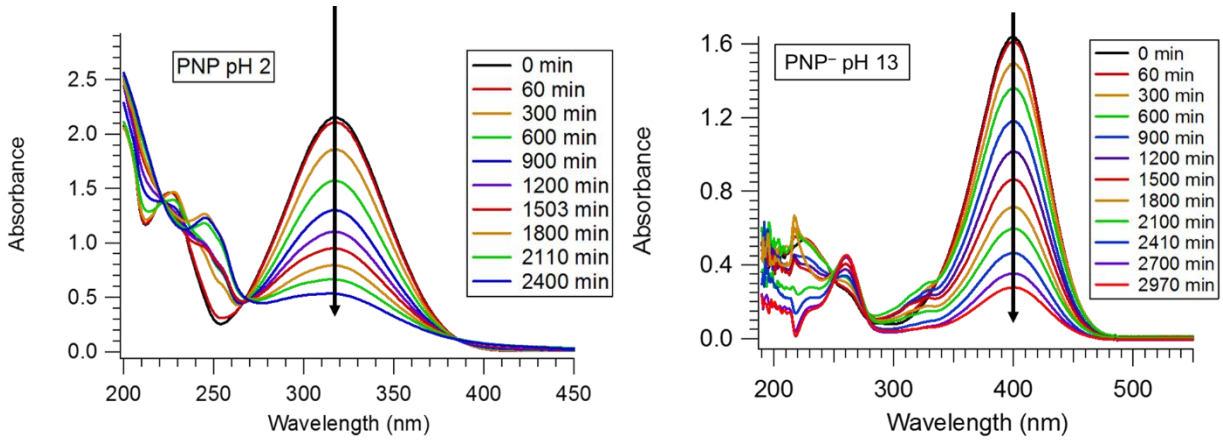

Figure 4-3: UV/Vis spectra collected at different irradiation times. Absorbance was recorded at 318 nm for PNP and at 400 nm for PNP^- as a measure of their concentrations in solution. The arrows denote the decrease of the peak over time.

these reactions were very slow, in the order of days, the irradiated sample and control were placed in the dark overnight on a number of occasions. Consequently, non-isosbestic behavior is observed in the spectra due to spontaneous reactions occurring between intermediate photoproducts. The difference in absorbance at the wavelengths associated with the target molecules between overnight cessations, however, was negligible. These variations were corrected by multiplying each absorbance value recorded for a given experimental period, defined as a period of continuous irradiation by the UV light source stopping only to collect a spectrum, $A_{p,n}$, by the ratio of the last absorbance recorded from the previous period, $A_{p-1,final}$, to the first absorbance recorded from

the current period, $A_{p,initial}$ (Eq. 4-10). In the notation, p refers to the collection period and n refers to each absorbance value obtained for that period.

$$A_{p,n,corrected} = \frac{A_{p,n}A_{p-1,final}}{A_{p,initial}} \quad \text{(Eq. 4-10)}$$

The percent concentration remaining was then calculated by dividing the absorbance of the degraded sample by the absorbance of the control. Plotting the percent concentration remaining as a function of irradiation time demonstrates that the photolysis is very slow, taking approximately 3800 minutes to decrease to around 5% remaining (Fig. 4-4). The initial rates were $(8.2 \pm 0.2) \times 10^{-10}$ mol L^{-1} s^{-1} after 240 minutes of irradiation for a 109 μM solution of PNP and $(6.9 \pm 0.2) \times 10^{-10}$ mol L^{-1} s^{-1} after 150 minutes of irradiation for a 129 μM solution of PNP^-.

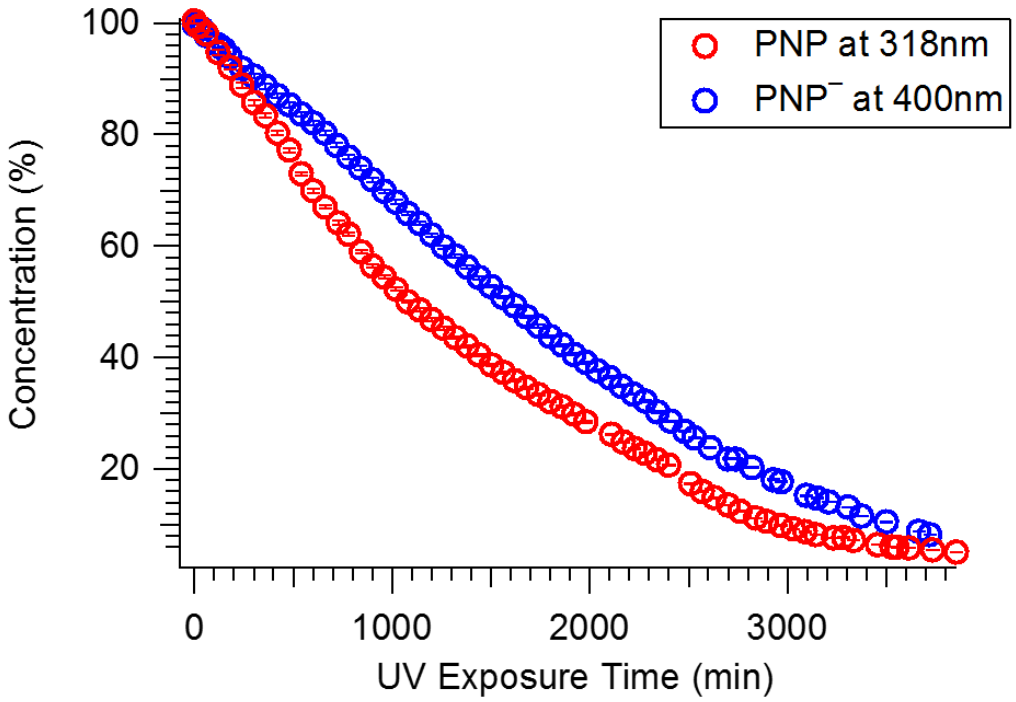

Figure 4-4: Percent concentration of PNP and PNP^- remaining as a function of UV exposure time.

As previously discussed, photochemical rates are dependent on the incident power of the UV light and the relative number of incident photons of each wavelength. The rate of

photodegradation may therefore be converted to a quantum efficiency, $\varphi_{\Delta\lambda}$, in order to quantify the photochemistry of these molecules[6] (Eq. 4-8 & 4-9).

For PNP, the quantum efficiency was calculated in the range of 200-400 nm, as the molecule absorbs less than one percent of the photons at wavelengths much longer than 400 nm. Using the results from the actinometry, a quantum efficiency of $(3.31 \pm 0.08) \times 10^{-5}\ \mathrm{mol\ einstein^{-1}}$ is reported. This value varies significantly from the quantum efficiency determined in this range by Bing *et al.*,[6] who report the quantum efficiency of the photolysis of PNP to be $7.94 \times 10^{-4}\ \mathrm{mol\ einstein^{-1}}$. However, the mercury arc lamp used in that experiment emits more photons of a shorter wavelength relative to the number of photons it emits at a higher wavelength, whereas the ozone free xenon arc lamp used in this study emits a greater number of photons of a longer wavelength than those of a shorter wavelength. In fact, only one third of the total incident photons from the UV lamp used in the present study are emitted in the range of 200-400 nm. Recalling the article by Alif *et al.*, which suggests that the quantum yield of PNP increases at shorter wavelengths[8], it is reasonable to assume that the quantum efficiency reported by Bing *et al.*[6] would be higher than those from this study, as quantum efficiency is a weight average.

In the same manner as for PNP, the quantum efficiency of PNP^- was calculated in the range of 200-480 nm, as less than one percent of the incident photons are absorbed by the molecule at wavelengths above 480 nm. A quantum efficiency of $(1.33 \pm 0.04) \times 10^{-5}\ \mathrm{mol\ einstein^{-1}}$ for this reaction was determined. As the quantum efficiency of PNP^- is about one third less than that of PNP, we may conclude that PNP^- is much more photostable, which is in accordance with the available literature.[6,8-10]

4.3 Surface Photochemistry of PNP⁻

The molecular orientations of the control sample and two samples undergoing irradiation by UV light were determined in the same manner as described earlier in this work. Plots of I_{SHG} as a function of the input polarization angle for each sample are shown for s- and p-output polarizations (Fig. 4-5). The p-output plot of the control sample, a sample kept in the dark on the

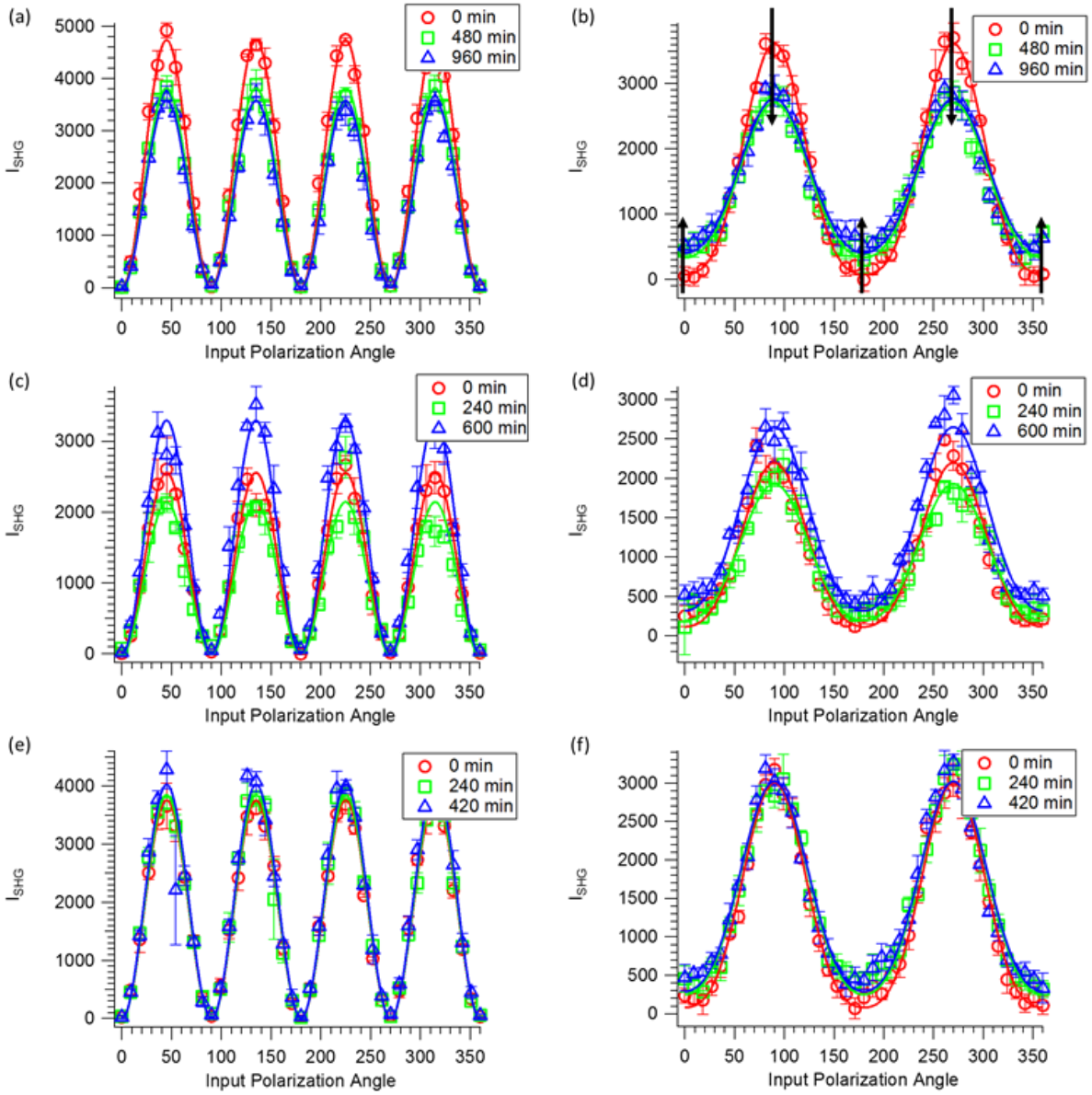

Figure 4-5: s-output (a,c,e) and p-output (b,d,f) plots of I_{SHG} versus input polarization angle for a control sample (a,b), and trial 1 (c,d) and trial 2 (e,f) of the photodegradation of PNP⁻ at the air water interface. The arrows in graph (b) represent the change in the features of the graph over time, which may be caused by acidification of the surface which would shift the equilibrium such that PNP⁻ ions adsorbed to the surface may protonate into PNP.

translation stage and exposed to room conditions for the duration of the experiment, shows that the SH intensity associated with p-input increases, whereas the SH intensity measured for s-input decreases as a function of time. In contrast, peak and trough intensities in both the p-output and s-output plots of the samples exposed to UV light seem to be relatively invariant over time or the change in SH intensity over time does not appear to follow a trend.

It is possible that these changes arise from a slow acidification of the interface as atmospheric carbon dioxide dissolves into the solution where it would form carbonic acid. If this hypothesis is valid, then the change in the features of the plot may be explained by either a change in the surface number density of PNP^- adsorbed to the interface, an orientational rearrangement of the adsorbed molecules, or a combination of the two. This is a reasonable conclusion, as these are the two surface properties that affect the magnitude of the SH intensity generated at the interface. A change in the surface pH may shift the equilibrium between PNP and PNP^- towards that of the neutral species such that that number of PNP^- ions at the surface decreases as they protonate to form PNP. The polarization dependent plots of the control sample may be reflective of this, as the changes in the features of the plot appear to be characteristic of PNP and indicate a reduction in the features associated with PNP^- (Fig. 3-2). However, the possibility exists that time dependent change in the features of the control sample are reflective of a change in the orientation of PNP^- at the surface which could be due to a reduction in the surface number density of PNP^- ions adsorbed to the interface or a change in the monolayer-substrate interactions. We may conclude, however, that any change in the SH signal in this experiment is due to a corresponding change in the PNP^- ions adsorbed to the surface as it provides a resonant contribution, whereas PNP does not.

A plot of the average molecular orientation of PNP^- as a function of time for the control sample shows that the molecule begins to shift to a configuration closer to the surface normal as the amount of time it is exposed to the atmosphere increases (Fig. 4-6). The same variation in orientation is shown to occur for both irradiated samples, which differ only in that trial 1 includes a data point reflective of irradiation over a longer period of time than trial 2 and is presented to reveal whether or not there is a change in the behavior of PNP^- over this longer time scale. Within the magnitude of the experimental uncertainty, there are no significant differences in the orientational behavior of PNP^- between the control and irradiated samples. As such, the reasons for this change may the same as those postulated previously to explain the time dependent change in the polarization plots of the control sample.

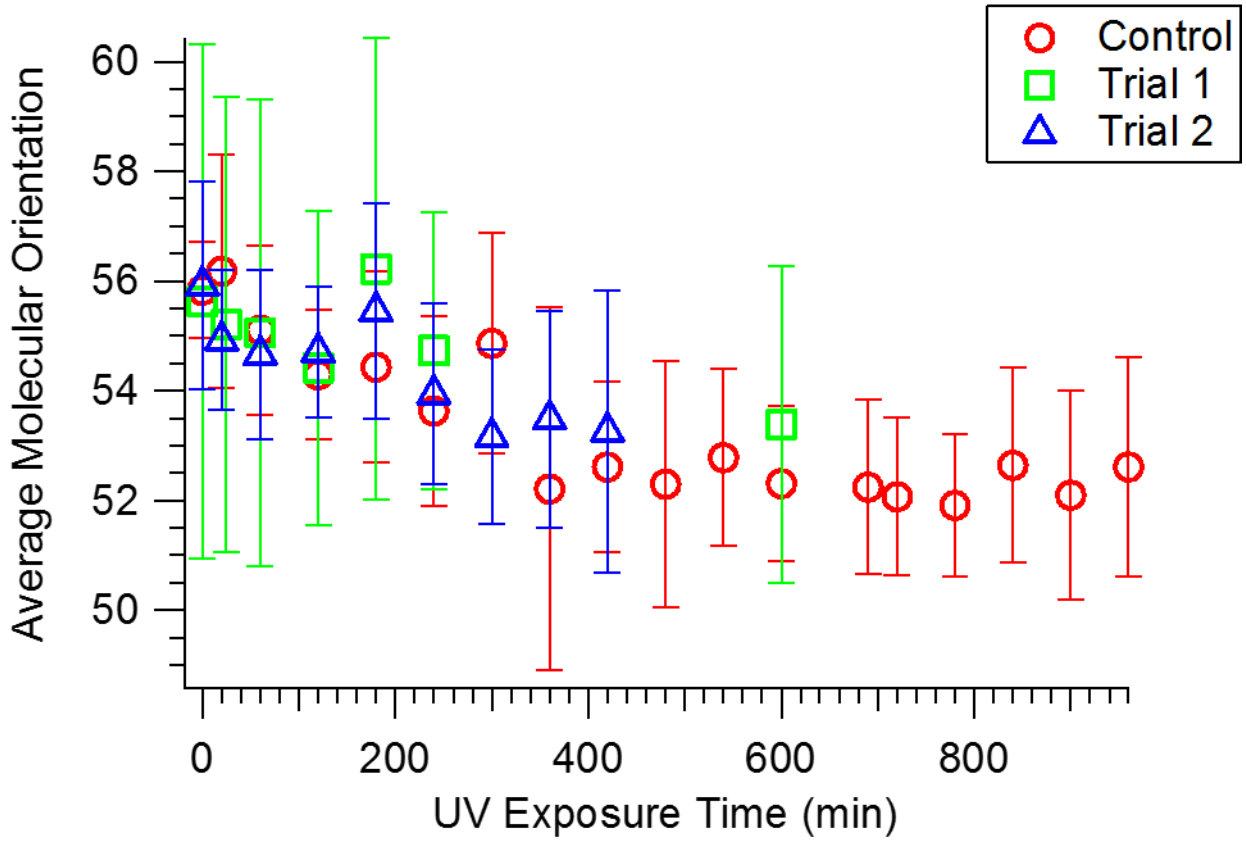

Figure 4-6: The average molecular orientation of the control sample and the two irradiated samples, begin to conform to an orientation that is closer to the surface normal.

Since the average molecular orientation of the adsorbate changes as a function of time, it is necessary to utilize the orientation insensitive polarization configuration to relate $\vec{E}_{SHG}$ to the number of adsorbed particles, specifically those with a resonant contribution, namely PNP^-. In the control, a decrease in SH field strength is observed which may be representative of the number of adsorbed PNP^- ions that have been converted into PNP (Fig. 4-7(a)). In contrast, the photodegraded samples either do not appear to change over time or show an increase in the SH field. If the interpretation of the orientation insensitive configuration is accurate, then what we observe is either no change to or an increase in the surface number density as the samples are irradiated.

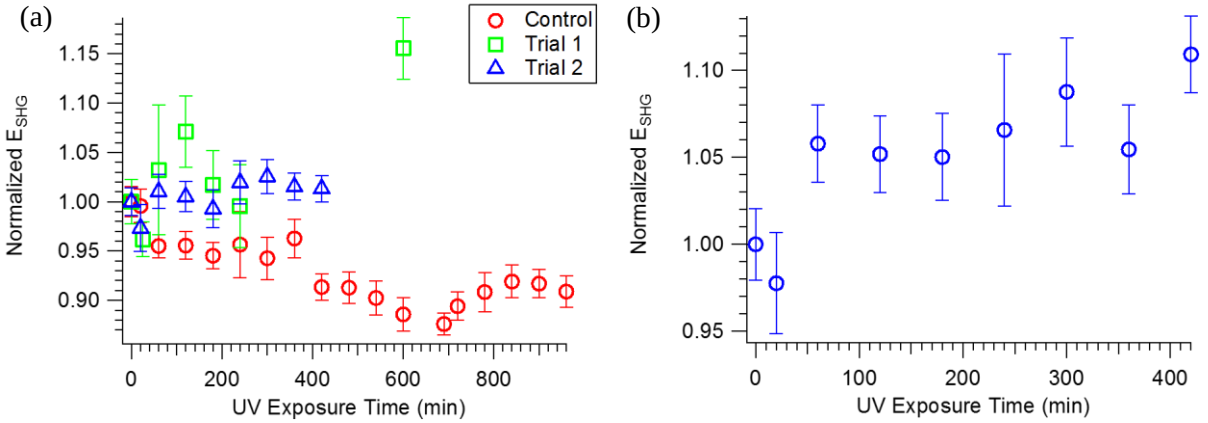

Figure 4-7: Normalized $\vec{E}_{SHG}$ plotted as a function of UV exposure time, simulated for the control, normalized from the first data point collected from each experiment (a), and normalized $\vec{E}_{SHG}$ of trial 2 (b), normalized with the control. In both plots, E_{SHG} was obtained using the orientation insensitive configuration. The decrease in SH field strength for the control sample is a representation of the number of PNP^- ions that may have been converted to PNP because of a change in the pH of the surface. The slight rise observed in the photolysis trials may indicate that there is no change in the surface number density of adsorbed PNP^- ions or that one or more of the photolysis products have an affinity for the surface.

This implies a number of possibilities. One is that the surface number density of PNP^- at the air-water interface is either not changing or increases slightly. This may be due to the orientation of the molecule at the surface, specifically that the nitro group is pointing out of the surface. This would reduce the probability of the denitration reaction, as any hydroxyl radicals generated would be less likely to access the carbon of the C-N bond. Another possibility is that

one or more of the photolysis products have an affinity to the air-water interface. If this is the case, it is either that a significant number of these products adsorb to the surface, or that one or more of them have a transition that is resonant with our laser. Of the reported photolysis products,[6,8] nitrocatechol is the most likely to contribute to SHG if adsorbed to the interface because it has a transition resonant with the SH frequency, however, it is not likely to be produced in high enough concentration to allow a significant number of these molecules to adsorb to the surface.

Irrespective of the reasons for the changes observed, a comparison of the photochemistry of the surface to that of the bulk is presented (Fig. 4-8). In the plot, the normalized $\vec{E}_{SHG}$ collected from the solution surface as it undergoes irradiation by UV light, and the normalized concentration from the bulk photodecomposition, are compared over a time span of 420 minutes. Over this period of time, the surface number density does not appear to change significantly within the magnitude of the experimental uncertainty, however, approximately 15% of the initial concentration of PNP^-

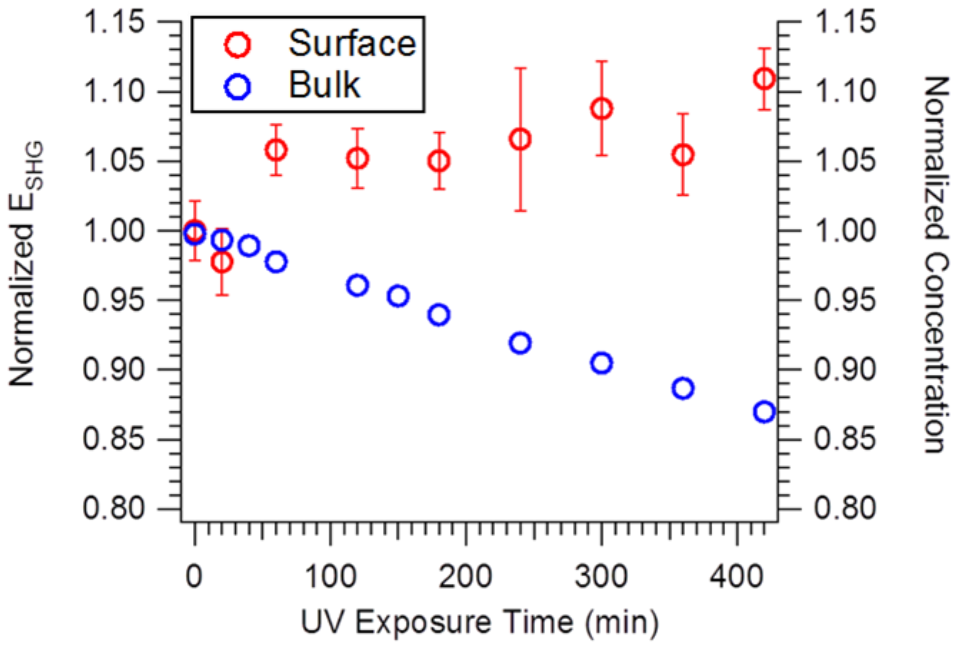

Figure 4-8: Normalized $\vec{E}_{SHG}$ from the surface and normalized concentration of the bulk plotted as a function of UV exposure time. From the graph, it can be concluded that the photochemistry of PNP^- at the air-water interface is slower than the bulk photolysis.

in the bulk solution has degraded. It may therefore be concluded that the photochemistry of PNP^- at the air-water interface is slower than that of the bulk under the experimental conditions utilized for this project.

References

(1) Aillet, T.; Loubiere, K.; Dechy-Cabaret, O.; Prat, L. Accurate measurement of the photon flux received inside two continuous flow microphotoreactors by actinometry. *International Journal of Chemical Reactor Engineering* **2014**, *12*, 257-269.

(2) Oriel Product Training - Spectral Irradiance. http://assets.newport.com/webdocuments-en/images/light_sources.pdf (2016).

(3) Calculating Output Power. https://www.newport.com/calculating-output-power (2016).

(4) Montalti, M.; Credi, A.; Prodi, L.; Gandolfi, M. T.: *Handbook of photochemistry*; CRC press, 2006.

(5) Hatchard, C.; Parker, C. A. In *Tilte*1956; The Royal Society.

(6) Bing, C.; Chun, Y.; Khang, G. Direct photolysis of nitroaromatic compounds in aqueous solutions. *Journal of Environmental Science (China)* **2005**, *17*, 598-604.

(7) Calvert, J. G.; Pitts, J. N. Photochemistry. **1966**.

(8) Alif, A.; Boule, P.; Lemaire, J. Comportement photochimique du nitro-4 phenol en solution aqueuse. *Chemosphere* **1987**, *16*, 2213-2223.

(9) Zhao, S.; Ma, H.; Wang, M.; Cao, C.; Xiong, J.; Xu, Y.; Yao, S. Study on the mechanism of photo-degradation of p-nitrophenol exposed to 254nm UV light. *Journal of hazardous materials* **2010**, *180*, 86-90.

(10) Zhao, S.; Ma, H.; Wang, M.; Cao, C.; Xiong, J.; Xu, Y.; Yao, S. Role of primary reaction initiated by 254 nm UV light in the degradation of p-nitrophenol attacked by hydroxyl radicals. *Photochemical & Photobiological Sciences* **2010**, *9*, 710-715.

Chapter 5: Conclusions and Future Work

5.1 Surface Equilibrium

The surface affinities of PNP and PNP^- in this study are reported to be higher than those reported in the literature for phenol[1-4] and phenolate,[2,4] respectively. This finding suggests that the nitro group drives the molecules to the solution surface. This is counter intutitve as the electron withdrawing effects should increase the overall polarity of the molecules, however, a recent study has reported nitro groups as having a hydration number of approximately zero.[5] The implication of this is that nitro groups do not form strong hydrogen bonding interactions with water molecules and is therefore considered hydroneutral, as opposed to hydrophilic. This hydroneutrality of the nitro group may be what drives PNP and PNP^- to the solution surface with a greater affinity than phenol and phenolate, respectively.

The orientational rearrangement of PNP^- potentially arises because of charge-charge or dipole-dipole interactions between anions adsorbed to the surface. Assuming that the molecules adsorbed to the surface are both sufficiently close to one another and that the magnitude of the net dipole or local charge densities are significant, the molecule may begin to rearrange into a configuration that is more parallel to the solution surface as they move closer to one another in proximity. If this is the case, however, application of the Langmuir isotherm model may not be justified as it assumes that the molecules adsorbing to the interface are non-interacting. It is also possible that the rearrangement observed arises from monolayer-substrate interactions, such that the molecular orbitals are interacting with the hydroxide ions in solution. This possibility is supported by observations of so-called “orientational fluctuations” in long-chain phenolate,

anilines, and *N*,*N*-dimethyl aniline.[6,7] In the study, the surface density of the molecules was adjusted and held constant while SHG measurements were taken as a function of time. While the method of measurement used in this study does not reveal the average molecular orientation, it does show that at certain surface number densities, different for each molecule, long-chain anilines dissolved in water, and long-chain phenolate dissolved in 2 N KOH undergo an orientational phase transition at the surface. In contrast, the same study found that long-chain phenols and long-chain aniliniums dissolved in 1 N HCl do not experience an orientational fluctuation. Furthermore, the study also precluded the possibility that the orientational fluctuation could be associated with a chain-chain interaction. In this study, they relate the chain-chain interaction to a frictional force that increases the time scale of the phase transition. Although these molecules are different from those used in this investigation, the forces influencing the orientational rearrangement are likely the same.

The red shift of the excitation wavelength from 400 nm to 408 nm may be due to a destabilization of the ground state of the molecule, a stabilization of the excited state, or related to Franck-Condon factors.[8] The source of this shift may be solvatochromatic, as the air-water interface has been shown to be analogous to a nonpolar solvent for a known polarity indicator, *N*,*N′*-diethyl-*p*-nitroaniline.[9] This may mean that the ground state of the molecule, which is polar, is destabilized due to the nonpolar quality of the surface, or that the excited state of the molecule is less polar than the ground state, thereby stabilizing the excited state at the interface. To explore this further, we intend to investigate the solvatochromatic behavior of PNP^- in bulk solution for comparison with the surface.

5.2 Surface Photochemistry of PNP^-

In our investigation, the photokinetic of PNP^- appears slower at the air-aqueous interface than in bulk solution. This may be explained by the orientation of the anion at the surface. In basic pH, the denitration reaction pathway is equally as likely as hydroxylation at the *ortho* position.[10-12] In order for denitration to proceed, the hydroxyl radical must have access to the carbon carrying the nitro group.[10,11] Since the orientation of PNP^- is such that the nitro group is pointing out of the solution,[13-15] it is less likely that the hydroxyl radical will be able to gain access to this carbon, which would effectively prevent the denitration reaction from occurring. Accordingly, the rate of photodegradation would be reduced as compared to that of the bulk solution.

It is interesting to note, however, that the orientation of PNP^- at the solution surface still changes under irradiation by UV light. It is still possible that the surface pH is changing, thereby shifting the equilibrium between PNP and PNP^- towards the neutral species. It is also possible that the orientational change experienced by PNP^- under irradiation is caused by a change in the chemical make-up of the bulk, assuming that the monolayer-substrate interaction is the primary reason for the orientational change of PNP^- at the air-aqueous interface. Similarly, if the orientational change observed in the control is attributed to dipole-dipole or charge-charge interactions at the surface, the orientational rearrangement could be attributed to the same change in the composition of the interface under irradiation.

5.3 Future Work

To investigate the equilibrium properties of phenolic compounds at the air-water interface further, *para*-substituted phenolic compounds with a variety of inductive effects should be studied, as well as phenolic compounds that form different charges in acidic and basic solutions. This would reduce the likelihood that the orientational rearrangement is caused by dipole-dipole or charge-

charge interactions. If a change in the average molecular orientation of molecules at the surface is observed only for molecules in alkaline solution, then we may conclude that the observed orientational change arises from a monolayer-substrate interaction with the metal cations or hydroxide anions in the bulk. Following this, we may investigate the effect of using different bases containing different cations. Our lab also intends to study the equilibrium of PNP^- at a hexane-water interface for comparison with this study. This is in an effort to understand how the equilibrium of PNP^- may change at this interface as well as to elucidate fundamental knowledge about this surface and how it differs from the air-water interface.

With respect to the photochemistry of PNP^- at the air-aqueous interface, performing the surface photodegradation for a longer time span would ensure that the surface has had sufficient exposure to the UV light source and confirm the result of this study. Due to the low quantum efficiency of the reaction, we will explore the possibility of using H_2O_2 as a catalyst for the reaction. Increasing the overall reaction rate will provide more insight into the photochemistry of the surface by reducing the number of uncontrolled variables that arise due to the long time scale of the reaction.

References

(1) Tamburello-Luca, A. A.; Hebert, P.; Brevet, P. F.; Girault, H. H. Resonant-surface second-harmonic generation studies of phenol derivatives at air/water and hexane/water interfaces. *J. Chem. Soc., Faraday Trans.* **1996**, *92*, 3079-3085.

(2) Rao, Y.; Subir, M.; McArthur, E. A.; Turro, N. J.; Eisenthal, K. B. Organic ions at the air/water interface. *Chemical Physics Letters* **2009**, *477*, 241-244.

(3) Castro, A.; Bhattacharyya, K.; Eisenthal, K. B. Energetics of adsorption of neutral and charged molecules at the air/water interface by second harmonic generation: Hydrophobic and solvation effects. *The Journal of chemical physics* **1991**, *95*, 1310-1315.

(4) Subir, M.: *Investigation of equilibrium and kinetic properties of charged and neutral molecules at the colloidal and the aqueous interfaces*; COLUMBIA UNIVERSITY, 2009.

(5) Sagawa, N.; Shikata, T. Are all polar molecules hydrophilic? Hydration numbers of nitro compounds and nitriles in aqueous solution. *Physical Chemistry Chemical Physics* **2014**, *16*, 13262-13270.

(6) Zhao, X.; Eisenthal, K. B. Monolayer orientational fluctuations and a new phase transition at the air water interface detected by second harmonic generation. *The Journal of chemical physics* **1995**, *102*, 5818-5826.

(7) Zhao, X.; Subrahmanyan, S.; Eisenthal, K. B. Orientational fluctuations and phase transitions of long chain molecules at the air/water interface. *Physical review letters* **1991**, *67*, 2025.

(8) Marini, A.; Munoz-Losa, A.; Biancardi, A.; Mennucci, B. What is solvatochromism? *The Journal of Physical Chemistry B* **2010**, *114*, 17128-17135.
(9) Wang, H.; Borguet, E.; Eisenthal, K. Polarity of liquid interfaces by second harmonic generation spectroscopy. *The Journal of Physical Chemistry A* **1997**, *101*, 713-718.
(10) Suarez, C.; Louys, F.; Günther, K.; Eiben, K. OH-radical induced denitration of nitrophenols. *Tetrahedron Letters* **1970**, *11*, 575-578.
(11) O'Neill, P.; Steenken, S.; van der Linde, H.; Schulte-Frohlinde, D. Reaction of OH radicals with nitrophenols in aqueous solution. *Radiation Physics and Chemistry (1977)* **1978**, *12*, 13-17.
(12) Alif, A.; Boule, P.; Lemaire, J. Comportement photochimique du nitro-4 phenol en solution aqueuse. *Chemosphere* **1987**, *16*, 2213-2223.
(13) Corn, R. M.; Higgins, D. A. Optical second harmonic generation as a probe of surface chemistry. *Chemical reviews* **1994**, *94*, 107-125.
(14) Higgins, D. A.; Abrams, M. B.; Byerly, S. K.; Corn, R. M. Resonant second harmonic generation studies of p-nitrophenol adsorption at condensed-phase interfaces. *Langmuir* **1992**, *8*, 1994-2000.
(15) Eisenthal, K. Liquid interfaces probed by second-harmonic and sum-frequency spectroscopy. *Chemical Reviews* **1996**, *96*, 1343-1360.

Appendix I: Modeling of the Surface

The method we used to model the air-water interface in our study is that of the nonlinear polarization sheet as described by Brevet *et al.*.[1] This model (Fig. A-1) treats the surface as a region with unique dielectrics, $\varepsilon_m(\omega)$ and $\varepsilon_m(2\omega)$, that is the average of the two linear optical dielectrics,

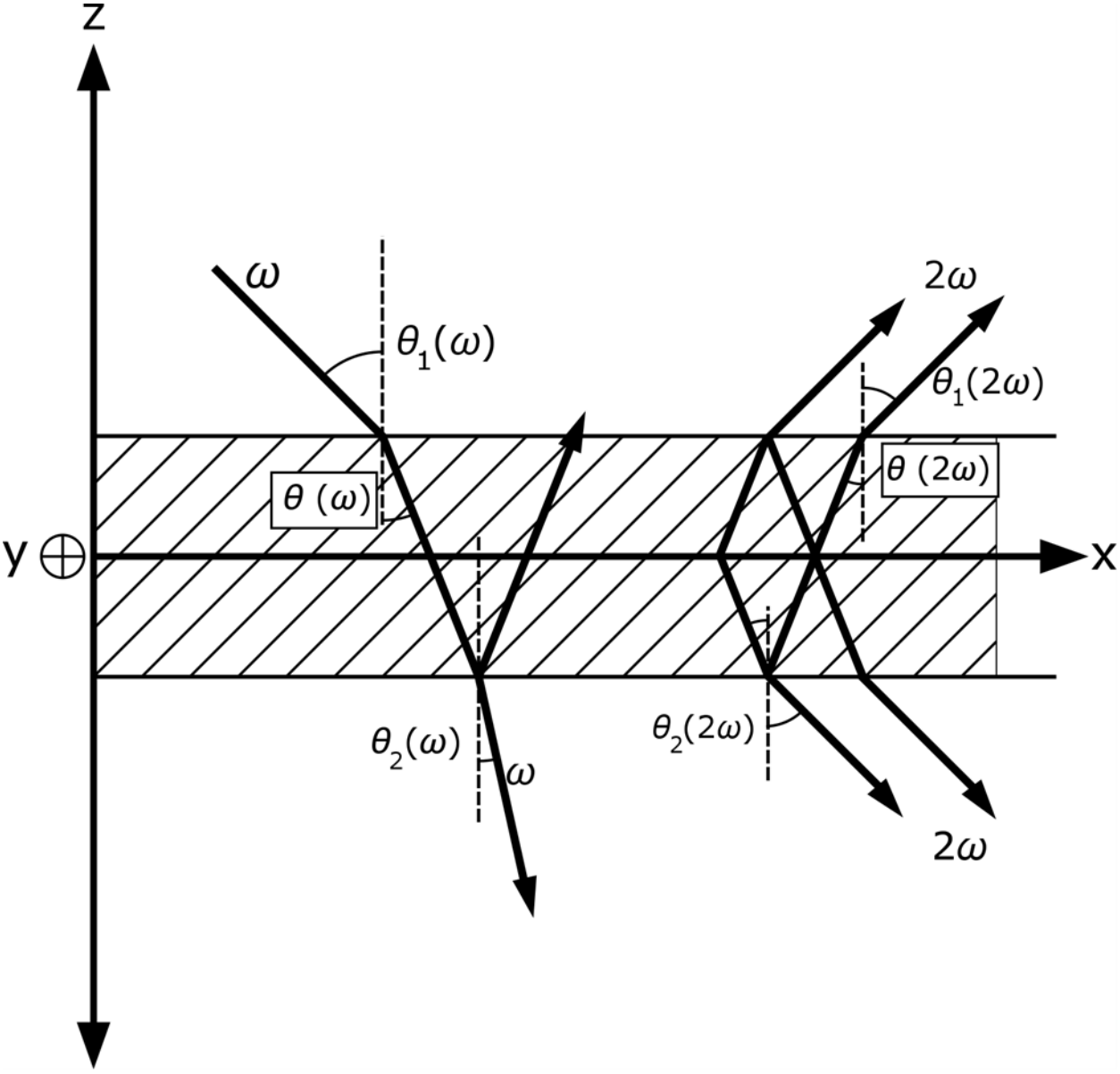

Figure A-1: Diagram of the nonlinear polarization sheet. In the figure, the bounded region denoted by diagonal lines represents the surface region, treated as a unique medium. Pictured above are multiple reflections and transmissions of both the fundamental, ω, and second harmonic, 2ω, beams.

$\varepsilon_1(\omega)$ and $\varepsilon_2(\omega)$, and $\varepsilon_1(2\omega)$ and $\varepsilon_2(2\omega)$, respectively. This model is used to calculate the a_i coefficients used in the determination of average molecular orientation and the orientation insensitive polarization configuration and is dependent upon the geometry.

In the reflection mode, the a_i coefficients (Eqs. A-1), where $i = 1 \ldots 5$, are calculated from the fundamental (Eqs. A-2) and harmonic unit vectors (Eqs. A-3), $e(\omega)$ and $e(2\omega)$, respectively.

$$\begin{aligned} a_1 &= e_y(\omega)e_z(\omega)e_y(2\omega) \\ a_2 &= -2e_z(\omega)e_x(\omega)e_x(2\omega) \\ a_3 &= e_x(\omega)e_x(\omega)e_z(2\omega) \\ a_4 &= e_z(\omega)e_z(\omega)e_z(2\omega) \\ a_5 &= e_y(\omega)e_y(\omega)e_z(2\omega) \end{aligned} \qquad \text{(Eqs. A-1)}$$

$$\begin{aligned} e_x(\omega) &= \left(r_{m2}^p - 1\right)t_{1m}^p \cos\theta(\omega) \\ e_y(\omega) &= (1 + r_{m2}^s)t_{1m}^s \\ e_z(\omega) &= \left(1 + r_{m2}^p\right)t_{1m}^p \sin\theta(\omega) \end{aligned} \qquad \text{(Eqs. A-2)}$$

$$\begin{aligned} e_x(2\omega) &= \left(R_{m2}^p - 1\right)T_{1m}^p \cos\theta(\omega) \\ e_y(2\omega) &= (1 + R_{m2}^s)T_{1m}^s \\ e_z(2\omega) &= \left(1 + R_{m2}^p\right)T_{1m}^p \sin\theta(\omega) \end{aligned} \qquad \text{(Eqs. A-3)}$$

The fundamental and harmonic vectors relate to the fractions of reflected and transmitted light, r and t, respectively, as they travel from one medium to another, where capital letters refer to the SH beam. In the equations above, s and p refer to s and p-polarized light, respectively. The angles $\theta(\omega)$ and $\theta(2\omega)$ refer to the angle between the surface normal and the fundamental and harmonic beam, respectively, within the nonlinear polarization sheet. The values of θ are determined from the experimental geometry and Snell's law (Eq. A-4), where n_1 and n_2 are the refractive indices of the two media that comprise interface.

$$n_1 \sin\theta_1 = n_2 \sin\theta_2 \qquad \text{(Eq. A-4)}$$

The Fresnel factors, r and t, are obtained from the dielectric constants of the media at the interface and the experimental geometry (Eqs. A-5, A-6, & A-7). In all equations, i and j refer to the media at the interface where, for our experiment, 1 is the air, m is the nonlinear polarization sheet, and 2 is the bulk solution.

$$r_{ij}^{s} = \frac{w_i - w_j}{w_i + w_j}$$
$$r_{ij}^{p} = \frac{w_i \varepsilon_j - w_j \varepsilon_i}{w_i \varepsilon_j + w_j \varepsilon_i} \qquad \text{(Eqs. A-5)}$$

$$t_{ij}^{s} = \frac{2w_i}{w_i + w_j}$$
$$t_{ij}^{p} = \frac{2w_i \sqrt{\varepsilon_i \varepsilon_j}}{w_i \varepsilon_j + w_j \varepsilon_i} \qquad \text{(Eqs. A-6)}$$

$$w_i = \sqrt{\varepsilon_i} \cos\theta_i \qquad \text{(Eq. A-7)}$$

The angle of incidence upon the surface in the experiment is 70° and the differences in the refractive indices of each material at 400 nm and 800 nm were negligible. Thus, the calculated a_i coefficients are as follows:

a_1	a_2	a_3	a_4	a_5
0.33923	-0.38455	0.19228	0.32011	0.33924

Table A-1: SHG orientational fitting coefficients for average molecular orientation calculations.

From these coefficients and for p-output polarized light, the orientation insensitive input polarization angle, γ^*, is calculated for a dominant $\beta_{z'z'z'}$ molecular hyperpolarizability[2] (Eq. A-8).

$$\gamma^* = \cos^{-1}\left(\frac{a_5}{3a_4 + a_5 - a_2 - a_3}\right)^{\frac{1}{2}} \qquad \text{(Eq. A-8)}$$

The geometry used in the experiments results in an orientation insensitive configuration of 61.5° input and p-output polarized light.

Appendix II: Confirmation of SH in Reflection Geometry

The Teflon dish from the surface SH experiments was replaced with a silver reference mirror because it provides a strong SH response. The mirror was not translated to minimize variations in the signal caused by imperfections on the surface of the mirror. The power incident on the mirror was adjusted by utilizing different combinations of neutral density filters. This procedure is carried out to optimize the detector and alignment, since the intensity of the SH is proportional to the square of the intensity of the fundamental beam (Eq. A-9)[1].

$$I_{2\omega} \propto I_{\omega}^{2} \qquad \text{(Eq. A-9)}$$

A plot of SH intensity versus input power (Fig. A-2) confirms that this relationship holds for input power readings below approximately 0.45 W, as the slope of the line from the log-log

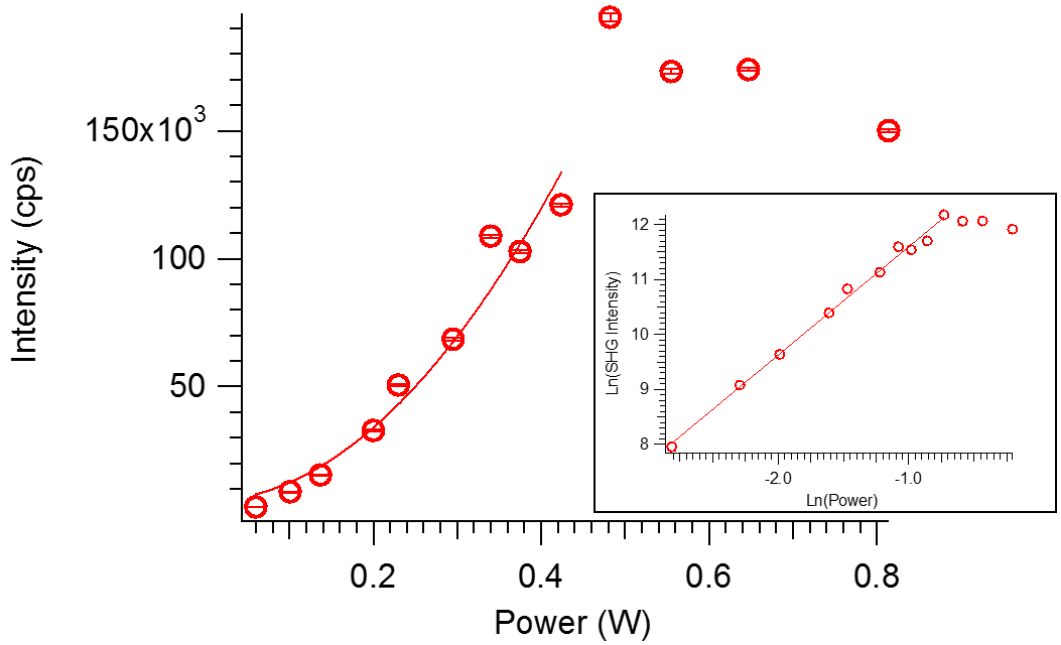

Figure A-2: SH intensity as a function of input power. The solid line is drawn to illustrate the quadratic dependence of the SH signal, $I_{2\omega}$, on the intensity of the fundamental beam, I_{ω}. The inset is that of the log-log plot of this relationship. The slope of the solid line in the inset is 2, which provides confidence that the measured signal is that of the SH.

plot of this relationship is 2 in this range. This plot also shows that for incident power above 0.45 W, processes other than SHG may be occurring, such as third-harmonic generation.

Appendix III: Confirmation of the SH Signal from a Solution of PNP^-

The same procedure as in Appendix II was carried out at a 45°-input and s-output polarization configuration for a sample of PNP^- that was translated in order to confirm that the signal generated from the surface of the solution was the SH signal. Plots of SH intensity as a function of incident power and the log-log plot of that relationship were generated (Fig. A-3). In the log-log plot, the slope of the line was 2.05 ± 0.03, confirming that the signal measured from the surface is the SH.

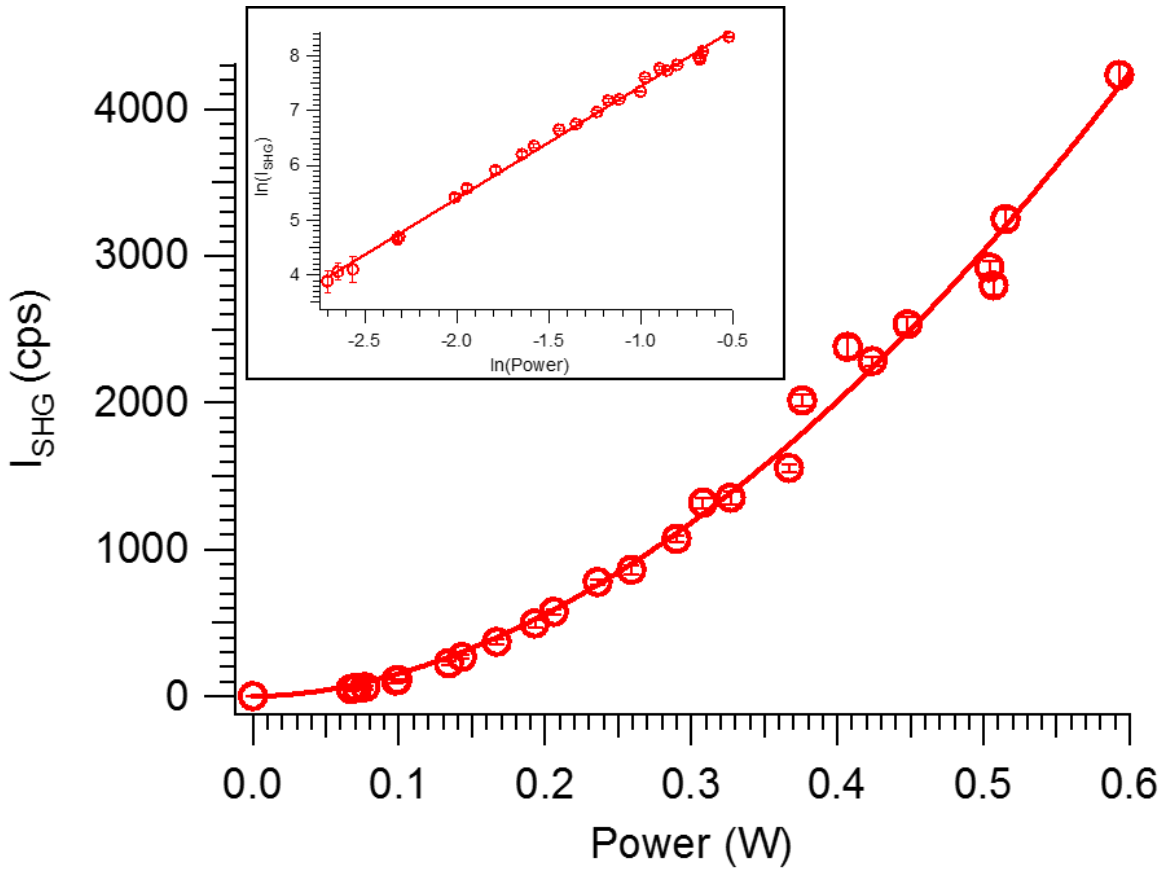

Figure A-3: SH intensity as a function of input power on a sample of PNP^- confirming that the signal generated at the surface is that of the SH.

Appendix IV: Standard Curve of Fe^{2+} Complexation with *o*-Phenanthroline

A standard curve of the iron (II) *o*-phenanthroline complex was produced using the method described in Chapter 2 (Fig. A-4). The molar extinction coefficient of this compound at 510 nm was found to be 11290 ± 20 dm^3 mol^{-1} cm^{-1}.

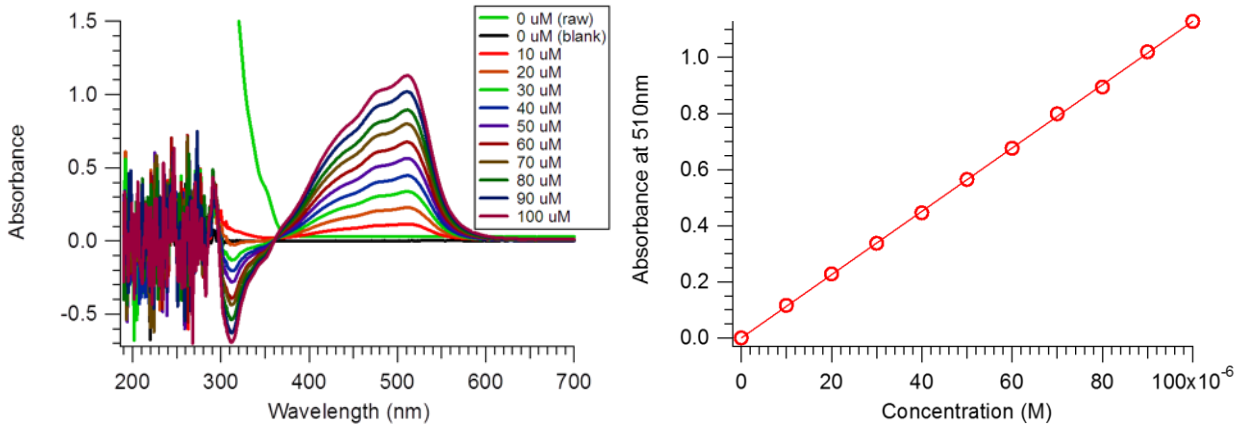

Figure A-4: Standard curve of the iron (II) *o*-phenanthroline complex. The absorbance spectra (left) of ten different concentrations were analyzed at 510 nm and plotted as a function of concentration (right). The slope of this line represents the molar extinction coefficient, which was 11290 ± 20 dm^3 mol^{-1} cm^{-1}.

Appendix V: Molar Extinction Coefficients of PNP and PNP^-

The molar extinction coefficients of PNP and PNP^- were determined from UV/Vis spectroscopy. Different concentrations of each solution were prepared and analyzed with a UV/Vis spectrometer. The extinction coefficients were found to be 19350 ± 50 dm^3 mol^{-1} cm^{-1} at 316 nm and 19420 ± 70 dm^3 mol^{-1} cm^{-1} at 401 nm, respectively.

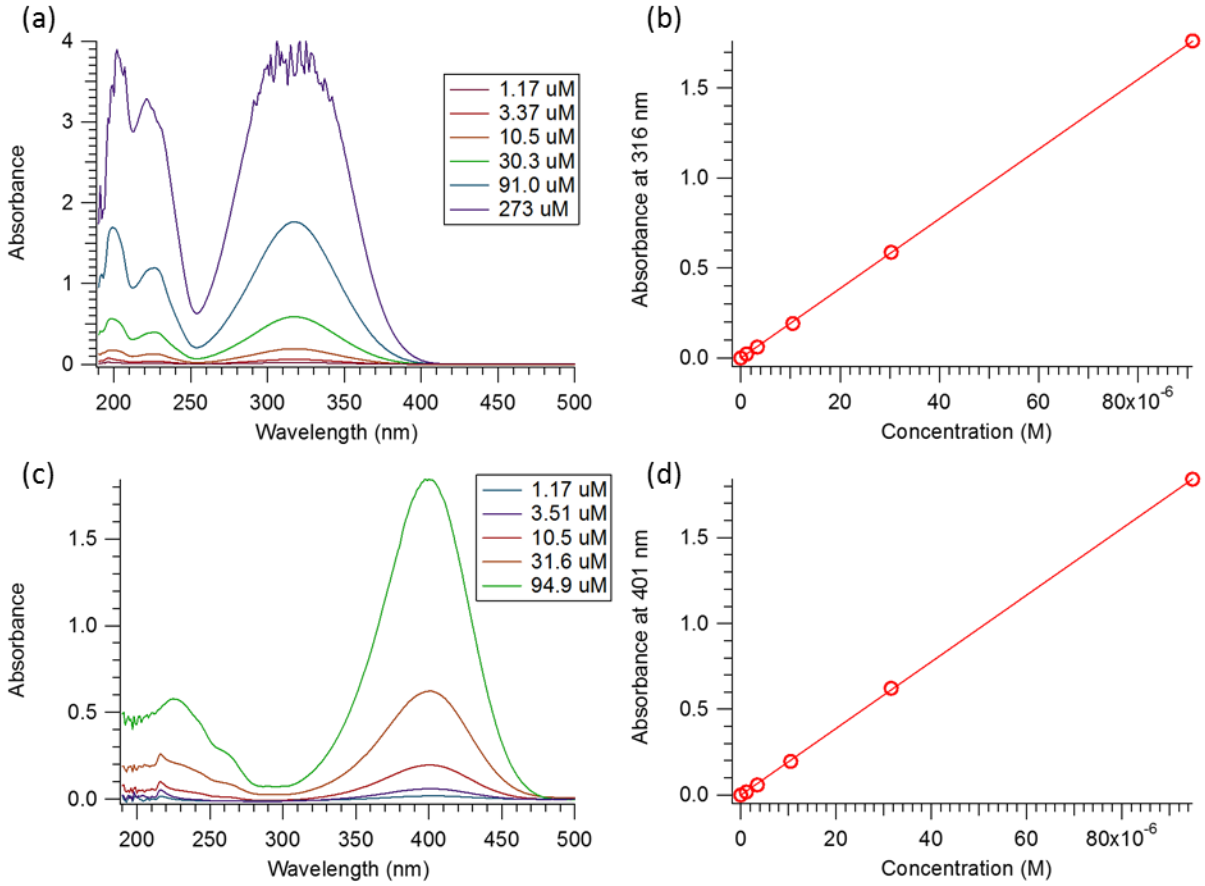

Figure A-5: UV/Vis spectra of PNP (a) and PNP^- (c) were analyzed at 316 and 401 nm, respectively. The resulting plots of absorbance as a function of concentration reveal the molar extinction coefficients to be 19350 ± 50 dm^3 mol^{-1} cm^{-1}, for PNP (b) and 19420 ± 70 dm^3 mol^{-1} cm^{-1}, for PNP^- (d).

Appendix VI: Modeling of the UV Lamp

The UV lamp used in the photochemical experiments was modeled in the manner described by Aillet *et al.*.[3] The spectral irradiance of the arc lamp, provided by the supplier,[4] was digitized, converted to a log plot, and then fit to an exponential as it provided a fit of the interpolated data (Fig. A-6) with a χ^2 of 0.0221503. The fit function was then converted back to spectral irradiance

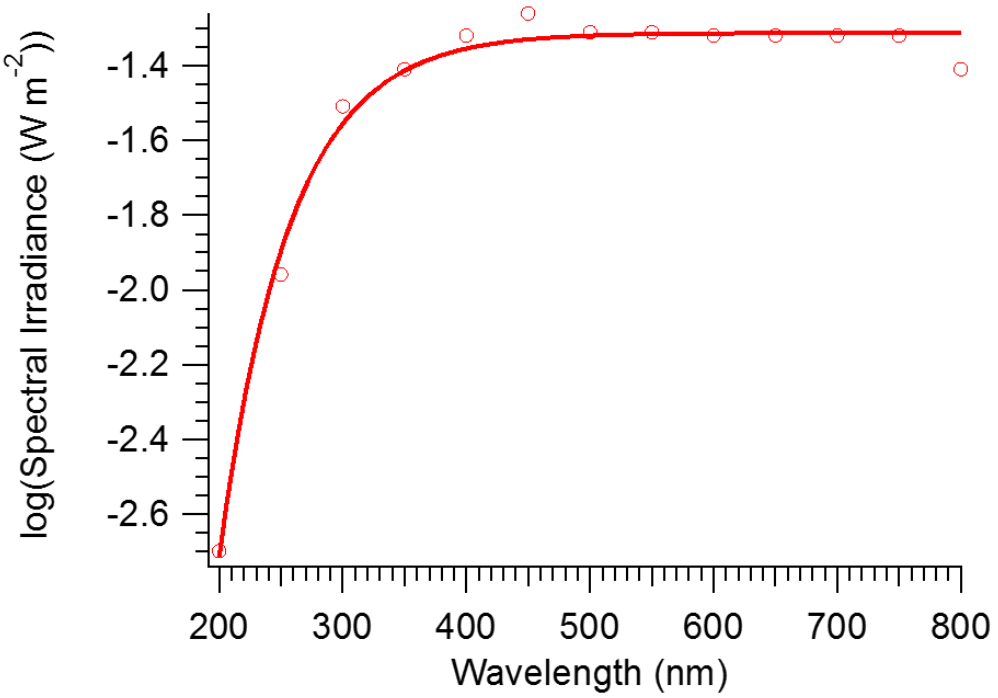

Figure A-6: The log plot of the interpolated spectral irradiance data. The exponential fit function used was in the form $y = y_0 + Ae^{-\tau\lambda}$. The fitting coefficients were $y_0 = -1.31 \pm 0.02$, $A = -50 \pm 10$, and $\tau = 0.018 \pm 0.001$.

with units of W m^{-2}. To correct for the F/1 condenser in the lamp housing, the spectral irradiance was multiplied by a factor of 0.11 for all wavelengths, as instructed by the supplier.[5] The correction used for the rear reflector in the lamp housing was multiplication by a factor of 1.2 for wavelengths below 250 nm which was then scaled linearly to a factor of 1.6 for wavelengths of 350 nm and above.[5] This process gives us the radiant exitance, $M_{e,\lambda}$, of the lamp for each wavelength in the

range of 200 to 550 nm. For each wavelength in this range, the radiant exitance was converted from energy quantities to photon quantities, $M_{p,\lambda}$, with units of einstein s^{-1} (Eq. A-10), using the wavelength, λ, Avogadro constant, N_A, Planck constant, h, and constant speed of light, c.

$$M_{p,\lambda} = M_{e,\lambda}\frac{\lambda}{N_A hc} \qquad \text{(Eq. A-10)}$$

These photon quantities were then converted to the density function of the lamp, g_λ, by dividing each photon quantity in the range of 200 to 500 nm by the sum of all the photon quantities in that range (Eq. A-11).

$$g_\lambda = \frac{M_{p,\lambda}}{\sum_{\lambda_i} M_{p,\lambda_i}} \qquad \text{(Eq. A-11)}$$

This function represents the relative number of photons emitted by the lamp per second. When the relative photon quantities are plotted as a function of wavelength, it is evident that the lamp used in the photochemistry experiments has a preponderance of photons of longer wavelengths as compared to those of shorter wavelengths (Fig. A-7).

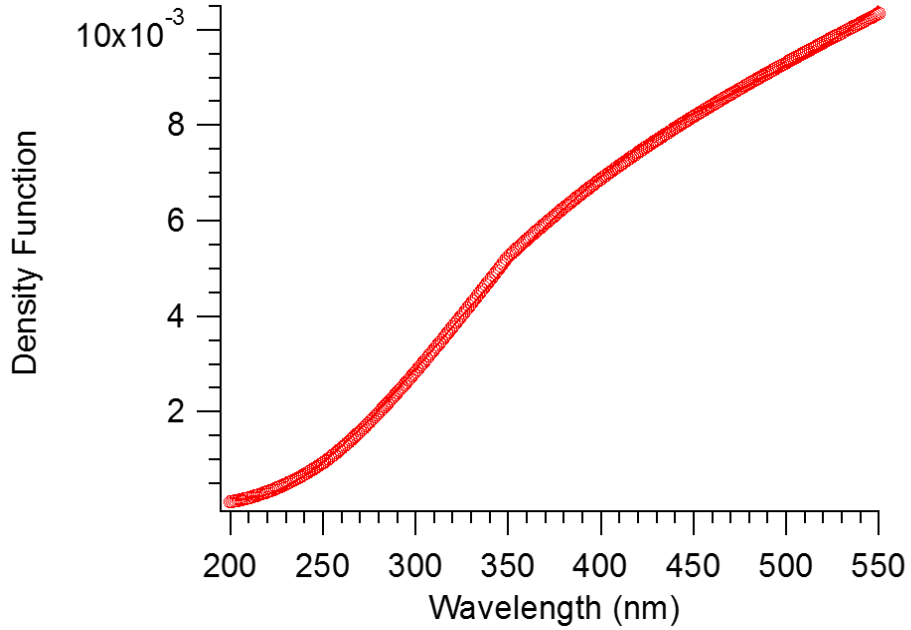

Figure A-7: The density function of the lamp, representing the relative number of photons of each wavelength emitted from the lamp per second, as a function of wavelength shows that the lamp used in the photochemistry experiments emits a greater number of photons of longer wavelengths compared to shorter ones.

Appendix VII: Interpolation of the Quantum Yield of Potassium Ferrioxalate

Quantum yield values of the potassium ferrioxalate actinometer obtained from literature[6-9] were plotted as a function of wavelength (Fig. A-8). From this plot, the quantum yield values were fit to a fourth order polynomial, $\Phi(\lambda)$, to interpolate quantum yield values for all wavelengths in

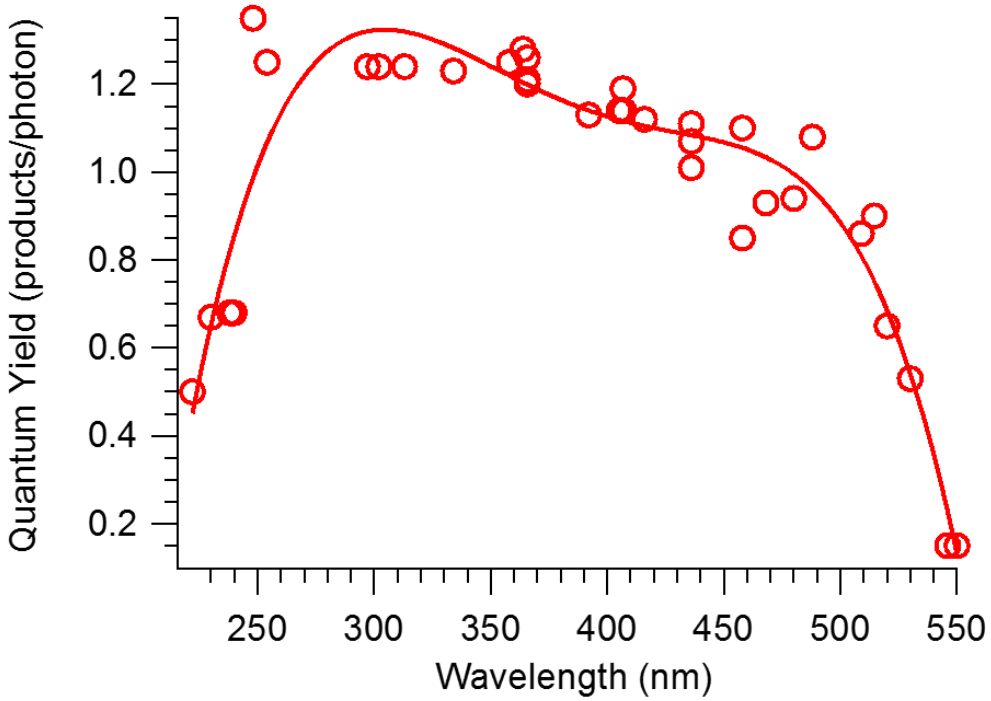

Figure A-8: Polynomial fit of the quantum yield values for the potassium ferrioxalate actinometer. The fit line was used to interpolate quantum yield information for each wavelength in the range of 200 to 550 nm.

the range of 200 to 550 nm (Eq. A-12). This method is similar to the one used by Bing *et al.*.[6] From the fit, wavelength, λ, is in nm, and the fitting coefficients, A_i, obtained are tabulated below (Table A-2).

$$\Phi_\lambda = A_0 + A_1\lambda + A_2\lambda^2 + A_3\lambda^3 + A_4\lambda^4 \qquad \text{(Eq. A-12)}$$

A_0	A_1	A_2	A_3	A_4
-38 ± 6	0.41 ± 0.07	$-(1.6 \pm 0.3) \times 10^{-3}$	$(2.8 \pm 0.5) \times 10^{-6}$	$-(1.8 \pm 0.3) \times 10^{-9}$

Table A-2: Coefficients obtained from the fourth order polynomial fit of quantum yield values from the literature.

Appendix VIII: Fraction of Light Absorbed by Potassium Ferrioxalate

In order to obtain the wavelength dependent fraction of light absorbed by the actinometer solution, f_λ, Napierian molar absorption coefficients, κ_λ, were interpolated from a graph published by Aillet *et al.*.[3] The information obtained from this graph was then fit to an exponential, and converted to the fraction of light absorbed using Eq. 4-3 (Fig. A-9).

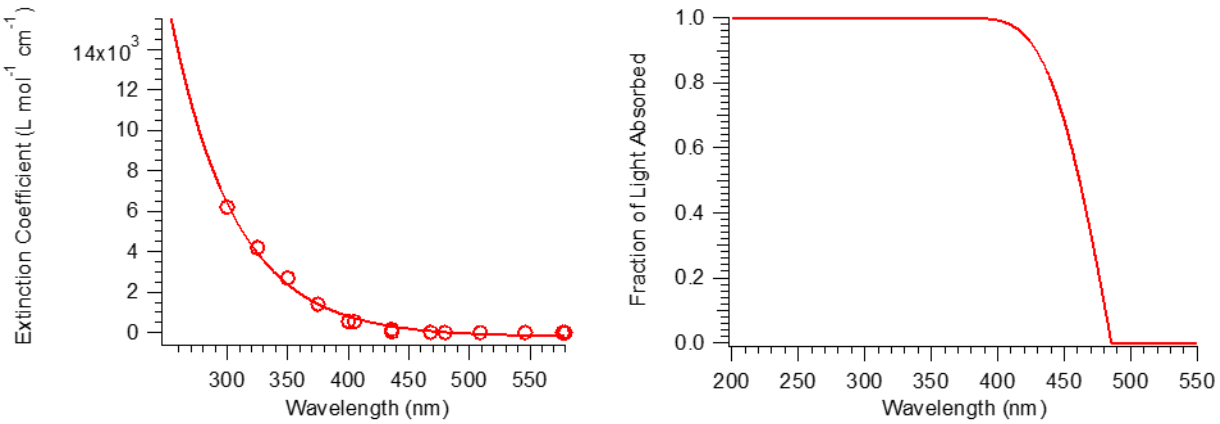

Figure A-9: The exponential fit line in the graph on the left was used to interpolate the Napierian molar absorption coefficient for each wavelength in the range of 200 to 550 nm. The fitting parameters were such that $y_0 = -200 \pm 100$, $A = (1.8 \pm 0.7) \times 10^6$, and $\tau = 0.019 \pm 0.001$, with the wavelength, λ, in nm. These molar absorption coefficients were then applied to Eq. 4-3 to obtain the fraction of light absorbed as shown in the graph on the right.

Appendix References

(1) Brevet, P. F.; Girault, H. H. Second harmonic generation at liquid/liquid interfaces. *Liquid-Liquid Interfaces: Theory and Methods. AG Volkov and DW Deamer, editors. CRC Press, Boca Raton, FL* **1996**, 103-137.

(2) Simpson, G. J.; Rowlen, K. L. Orientation-insensitive methodology for second harmonic generation. 1. Theory. *Analytical chemistry* **2000**, *72*, 3399-3406.

(3) Aillet, T.; Loubiere, K.; Dechy-Cabaret, O.; Prat, L. Accurate measurement of the photon flux received inside two continuous flow microphotoreactors by actinometry. *International Journal of Chemical Reactor Engineering* **2014**, *12*, 257-269.

(4) Oriel Product Training - Spectral Irradiance. http://assets.newport.com/webdocuments-en/images/light_sources.pdf (2016).

(5) Calculating Output Power. https://www.newport.com/calculating-output-power (2016).

(6) Bing, C.; Chun, Y.; Khang, G. Direct photolysis of nitroaromatic compounds in aqueous solutions. *Journal of Environmental Science (China)* **2005**, *17*, 598-604.

(7) Calvert, J. G.; Pitts, J. N. Photochemistry. **1966**.

(8) Montalti, M.; Credi, A.; Prodi, L.; Gandolfi, M. T.: *Handbook of photochemistry*; CRC press, 2006.

(9) Hatchard, C.; Parker, C. A. In *Tilte*1956; The Royal Society.